

Not Just How Much, But Where: Decomposing Epistemic Uncertainty into Per-Class Contributions

Mame Diarra Toure¹

David A. Stephens¹

¹Department of Mathematics and Statistics, McGill University

Abstract

In safety-critical classification, the cost of failure is often asymmetric. Yet Bayesian deep learning summarises epistemic uncertainty with a single scalar, mutual information (MI), which cannot distinguish whether a model’s ignorance involves a benign or safety-critical class. We decompose MI into a per-class vector $C_k(x) = \sigma_k^2 / (2\mu_k)$, with $\mu_k = \mathbb{E}[p_k]$ and $\sigma_k^2 = \text{Var}[p_k]$ across posterior samples. The decomposition follows from a second-order Taylor expansion of the entropy; the $1/\mu_k$ weighting corrects boundary suppression and makes C_k comparable across rare and common classes. By construction $\sum_k C_k \approx \text{MI}$, and a companion skewness diagnostic flags inputs where the approximation degrades. After characterising the axiomatic properties of C_k , we validate it on three tasks: (i) selective prediction for diabetic retinopathy, where critical-class C_k reduces selective risk by 34.7% over MI and 56.2% over variance baselines; (ii) out-of-distribution detection on clinical and image benchmarks, where $\sum_k C_k$ achieves the highest AUROC and the per-class view exposes asymmetric shifts invisible to MI; and (iii) a controlled label-noise study in which $\sum_k C_k$ shows less sensitivity to injected aleatoric noise than MI under end-to-end Bayesian training, while both metrics degrade under transfer learning. Across all tasks, the quality of the posterior approximation shapes uncertainty at least as strongly as the choice of metric, suggesting that how uncertainty is propagated through the network matters as much as how it is measured.

metric: missing a sight-threatening retinal condition is categorically different from a false positive; auto-allowing hate speech carries risks that auto-blocking benign content does not. Bayesian deep learning addresses this by maintaining a posterior over model parameters, enabling principled decomposition of predictive uncertainty into *aleatoric* (irreducible data noise) and *epistemic* (model ignorance, reducible with data) components. The foundational decomposition was formalised by Kendall and Gal [2017] for vision tasks and by Depeweg et al. [2018] for latent-variable models via the law of total variance; Lakshminarayanan et al. [2017] established deep ensembles as a scalable alternative to variational inference, with Gustafsson et al. [2020] demonstrating empirically that ensembles provide more reliable, better-calibrated uncertainty estimates than MC dropout across synthetic-to-real transfer benchmarks.

All of these methods, however, summarise epistemic uncertainty with a *single scalar per input*: the mutual information $\mathcal{I}(y; \omega | x) = H(\mu) - \mathbb{E}[H(p)]$ [Houlsby et al., 2011, Gal and Ghahramani, 2016]. This scalar reveals *how uncertain* the model is, but not *which classes* are driving that uncertainty, a distinction that matters because model ignorance is rarely distributed uniformly across the label space. A scalar MI of 0.3 nats carries very different implications depending on whether the confusion involves two benign classes or a benign and a safety-critical one.

Recent work has approached the per-class direction from several angles, each with a specific limitation (detailed comparison in Appendix A). Sale et al. [2024] introduced a label-wise framework reducing K -class problems to K binary sub-problems, with per-class epistemic variance $\text{EU}_k = \text{Var}(\Theta_k)$ satisfying strong axiomatic properties [Wimmer et al., 2023]; however, raw variance suffers from *boundary suppression*, the constraint $\text{Var}[p_k] \leq \mu_k(1 - \mu_k)$ forces it to vanish for rare classes regardless of actual posterior disagreement. Dirichlet-based approaches [Sensoy et al., 2018, Malinin and Gales, 2018, Duan et al., 2024] produce per-class epistemic covariances in a single forward pass, but impose a strong distributional assumption on the proba-

1 INTRODUCTION

Deep learning classifiers deployed in safety-critical domains operate in environments where the cost of failure is *asym-*

bility simplex. Dataset-level methods [Baltaci et al., 2023, Khan et al., 2019] address class imbalance and difficulty but conflate aleatoric and epistemic components and cannot provide input-level attribution. Scalar epistemic metrics, including BALD [Houlsby et al., 2011] for active learning and the variance-MI connection of Smith and Gal [2018], remain agnostic to class identity. Mucsányi et al. [2024] observed that aleatoric and epistemic estimates are often rank-correlated; de Jong et al. [2026] prove this is a necessary consequence of estimator validity, shifting the defining criterion from decorrelation to *orthogonality*, a property that no current method fully achieves.

In summary, no existing method provides an input-specific, normalised per-class epistemic vector with a direct additive connection to MI.

We introduce $\mathbf{C}(x) = [C_1(x), \dots, C_K(x)]^\top$, where $C_k(x) = \frac{1}{2} \text{Var}[p_k](x) / \mu_k(x)$ is derived from a second-order Taylor approximation of MI (Section 2). The $1/\mu_k$ normalization arises naturally from the entropy Hessian and counteracts boundary suppression; by construction, $\sum_k C_k(x) \approx \mathcal{I}(y; \omega | x)$, so each C_k attributes a well-defined share of total epistemic uncertainty to class k .

Contributions. (1) We derive $\mathbf{C}(x)$ from the Taylor expansion of MI (Section 2.1), characterise its axiomatic properties relative to Wimmer et al. [2023] (Section 2.4), and introduce a skewness diagnostic that flags when the approximation degrades (Section 2.5). (2) We validate $\mathbf{C}(x)$ across three tasks: selective prediction with class-specific deferral for diabetic retinopathy (Section 3), OoD detection where per-class contributions reveal asymmetric distributional shift (Section 4), and a controlled disentanglement study showing that $\sum_k C_k$ is less sensitive to injected label noise than MI under end-to-end Bayesian training, while both metrics degrade substantially under transfer learning (Section 5)¹.

2 PER-CLASS EPISTEMIC UNCERTAINTY

We decompose MI into a per-class vector via a second-order Taylor expansion of the entropy function (Sections 2.1–2.2), show that the decomposition corrects a pathology of raw variance near the simplex boundary (Section 2.3), characterise its axiomatic properties (Section 2.4), and introduce a diagnostic that flags when the approximation degrades (Section 2.5).

Setup and Notation Consider a K -class classifier with input x . We perform S stochastic forward passes (e.g.,

¹Concurrently, de Jong et al. [2026] show that pretrained deep ensembles exhibit worse AU/EU disentanglement than models trained from scratch, a conclusion we reach independently in Section 5 via both the degradation of the C_k approximation and increased AU/EU entanglement under transfer learning.

MC dropout, posterior sampling, or ensemble members), each producing a probability vector $\mathbf{p}^{(s)}(x) = \text{softmax}(\mathbf{z}^{(s)}(x)) \in \Delta^{K-1}$, where $\mathbf{z}^{(s)}$ denotes the logits from pass s . The Monte Carlo estimates of the mean and covariance are:

$$\boldsymbol{\mu}(x) = \frac{1}{S} \sum_{s=1}^S \mathbf{p}^{(s)}(x), \quad (1)$$

$$\text{Cov}[\mathbf{p}] = \frac{1}{S-1} \sum_{s=1}^S (\mathbf{p}^{(s)} - \boldsymbol{\mu})(\mathbf{p}^{(s)} - \boldsymbol{\mu})^\top, \quad (2)$$

with diagonal elements $\text{Var}[p_k] = \frac{1}{S-1} \sum_s (p_k^{(s)} - \mu_k)^2$. Throughout we rely on the standard decomposition

$$\underbrace{H(\boldsymbol{\mu})}_{\text{Total}} = \underbrace{\mathbb{E}[H(\mathbf{p})]}_{\text{Aleatoric}} + \underbrace{H(\boldsymbol{\mu}) - \mathbb{E}[H(\mathbf{p})]}_{\text{Epistemic } (\mathcal{I})}, \quad (3)$$

where $H(\mathbf{p}) = -\sum_k p_k \log p_k$ is the Shannon entropy and the epistemic term equals the mutual information $\mathcal{I}(y; \omega | x)$.

2.1 FROM SCALAR MI TO A PER-CLASS DECOMPOSITION

Our strategy is to approximate $\mathbb{E}[H(\mathbf{p})]$ via a Taylor expansion around $\boldsymbol{\mu}$, which yields an expression for MI that decomposes additively over classes.

Lemma 2.1 (Entropy Derivatives). *The Shannon entropy $H(\mathbf{p}) = -\sum_k p_k \log p_k$ satisfies*

$$\frac{\partial H}{\partial p_k} = -1 - \log p_k, \quad \frac{\partial^2 H}{\partial p_k \partial p_j} = -\frac{\delta_{kj}}{p_k}, \quad \frac{\partial^3 H}{\partial p_k^3} = \frac{1}{p_k^2}. \quad (4)$$

where δ_{kj} is the Kronecker delta ($\delta_{kj} = 1$ if $k = j$, 0 otherwise).

The Hessian is diagonal and negative definite on the interior of the simplex. The diagonal Hessian is what makes a per-class decomposition possible: there are no cross-class terms at second order, so the quadratic approximation splits cleanly over classes.

Theorem 2.2 (MI Approximation). *Let $\mathbf{p}^{(s)} \sim Q$ with mean $\boldsymbol{\mu} = \mathbb{E}_Q[\mathbf{p}]$ and per-class variance $\text{Var}[p_k]$. Then*

$$\mathbb{E}_Q[H(\mathbf{p})] \approx H(\boldsymbol{\mu}) - \frac{1}{2} \sum_{k=1}^K \frac{\text{Var}[p_k]}{\mu_k}, \quad (5)$$

with remainder $O(\mathbb{E}[\|\mathbf{p} - \boldsymbol{\mu}\|^3])$, and consequently

$$\mathcal{I}(y; \omega | x) \approx \frac{1}{2} \sum_{k=1}^K \frac{\text{Var}[p_k](x)}{\mu_k(x)}. \quad (6)$$

The simplex constraint forces $\text{Cov}[\mathbf{p}]$ to rank $K-1$, coupling the K components; this does not invalidate the trace formula. See Appendix B.1 for proof.²

²Smith and Gal [2018] also exploit a Taylor expansion to relate softmax variance to MI, but expand the *logarithm* $\log p_k$ rather than the entropy function $H(\mathbf{p})$ itself (their Section 3.2, Eq. 10). This yields a class-averaged variance $\frac{1}{K} \sum_k \text{Var}[p_k]$ with equal weights per class, whereas expanding the entropy via its Hessian yields the curvature-weighted sum $\frac{1}{2} \sum_k \text{Var}[p_k] / \mu_k$, in which the $1/\mu_k$ factor enables per-class attribution.

2.2 PER-CLASS EPISTEMIC UNCERTAINTY VECTOR

The additive structure of (6) invites a natural definition.

Definition 2.3 (Per-Class Epistemic Uncertainty). For a K -class classifier with mean $\mu(x)$ and per-class variance $\text{Var}[p_k](x)$ from S stochastic forward passes, define the **per-class epistemic uncertainty vector** $C(x) = [C_1(x), \dots, C_K(x)]^\top$ with

$$C_k(x) := \frac{1}{2} \frac{\text{Var}[p_k](x)}{\mu_k(x)}, \quad (7)$$

In practice, we add $\varepsilon = 10^{-10}$ to the denominator for numerical stability.³ When $\mu_k = 0$ across all passes, $\text{Var}[p_k] = 0$ and $C_k = 0$ trivially.

By construction, the vector satisfies

$$\sum_{k=1}^K C_k(x) \approx \mathcal{I}(y; \omega | x). \quad (8)$$

so each C_k attributes a well-defined share of total epistemic uncertainty to class k , providing the localisation that scalar MI lacks.

2.3 WHY VARIANCE ALONE FAILS: BOUNDARY SUPPRESSION

A natural alternative to C_k would be to use the raw variance $\text{Var}[p_k]$ as a per-class epistemic measure, as proposed by Sale et al. [2024]. However, variance on a bounded interval exhibits a structural limitation near the simplex boundary that the $1/\mu_k$ normalisation in (7) is designed to address.

Lemma 2.4 (Variance Bound on the Simplex). *For any class k with mean prediction $\mu_k \in [0, 1]$:*

$$\text{Var}[p_k] \leq \mu_k(1 - \mu_k). \quad (9)$$

Consequently, $\text{Var}[p_k] \rightarrow 0$ as $\mu_k \rightarrow 0$ or $\mu_k \rightarrow 1$, regardless of the degree of model disagreement in logit space. See Appendix B.2.

This bound reveals a concrete problem: for a class with $\mu_k \approx 0.01$, variance is capped at roughly 0.01 even if the model’s stochastic passes exhibit maximal disagreement about that class. The following lemma shows that C_k corrects exactly this pathology.

³The ratio $\text{Var}[p_k]/\mu_k$ coincides with the *index of dispersion* [Cox and Lewis, 1966] (Fano factor [Fano, 1947]). Here the $\frac{1}{2}$ prefactor and the $1/\mu_k$ weighting both emerge from the entropy Taylor expansion, so the components sum to a well-defined information-theoretic quantity.

Lemma 2.5 (Boundary Behaviour of C_k). *Under the same conditions:*

$$C_k = \frac{1}{2} \frac{\text{Var}[p_k]}{\mu_k} \leq \frac{1}{2}(1 - \mu_k), \quad (10)$$

which approaches $\frac{1}{2}$ (not zero) as $\mu_k \rightarrow 0$. The contrast is stark: while $\text{Var}[p_k]$ is crushed to zero near the simplex boundary, C_k retains a non-vanishing upper bound. See Appendix B.2.

The mechanism is not ad hoc: the Hessian entry $-1/\mu_k$ grows large when μ_k is small, so a given amount of probability variance carries more information-theoretic weight for low-probability classes. Conversely, when $\mu_k \rightarrow 1$ the curvature vanishes and $C_k \rightarrow 0$, the correct limit. This renders C_k comparable across classes with very different base rates, a property $\text{Var}[p_k]$ lacks by construction.

2.4 AXIOMATIC ANALYSIS

Having described both the diagonal vector $C(x)$ and the off-diagonal covariance structure, we now examine whether $C(x)$ satisfies standard properties of epistemic uncertainty measures. Wimmer et al. [2023] propose a set of axioms formalising desirable behaviour for epistemic uncertainty measures. We assess the aggregate $\text{EU}_{\text{approx}}(Q) = \sum_k C_k$ against five of these axioms, where Q denotes the second-order distribution over probability vectors p with mean $\mu = \mathbb{E}_Q[p]$.

Theorem 2.6 (Axiomatic Profile). *The approximate epistemic uncertainty $\text{EU}_{\text{approx}}(Q) = \sum_{k=1}^K C_k$ satisfies axioms A0, A1, and A3, and violates A2 and A5 of Wimmer et al. [2023]. See Appendix B.3 for details and proof.*

The violations of A2 and A5 are not artefacts of the approximation; they are inherited from MI itself [Wimmer et al., 2023]. More revealing is the relationship between A5 and boundary suppression:

Corollary 2.7 (A5 Violation as Boundary Correction). *The violation of A5 is the precise mechanism that counteracts boundary suppression. A5 requires EU to be insensitive to μ_k ; but by Lemma 2.5, sensitivity to μ_k is what prevents C_k from vanishing as $\mu_k \rightarrow 0$.*

This trade-off clarifies the design space: the label-wise variance $\text{EU}_k = \text{Var}(\Theta_k)$ of Sale et al. [2024] satisfies A5 but pays the cost of boundary suppression. Our C_k sacrifices A5 to preserve comparability across classes with different base rates, a trade-off we argue is favourable in safety-critical settings where rare classes matter most.

Remark 2.8 (A3 vs. Exact MI). Unlike exact MI, which Wimmer et al. [2023] show violates A3 in general (their Proposition 4), $\sum_k C_k$ satisfies it strictly. Since the sum

is linear in each $\text{Var}[p_k]$ with fixed positive coefficients $1/(2\mu_k)$, any mean-preserving spread necessarily increases it, so greater model disagreement always produces greater epistemic uncertainty.

2.5 RELIABILITY DIAGNOSTIC VIA SKEWNESS

The same $1/\mu_k$ factor that corrects boundary suppression also controls where the Taylor expansion breaks down. As $\mu_k \rightarrow 0$, the curvature $|\partial^2 H/\partial p_k^2| = 1/\mu_k$ diverges, and the quadratic approximation becomes increasingly sensitive to higher-order terms. A natural question is: *when can we trust C_k ?* We answer this by examining the next term in the expansion.

Lemma 2.9 (Third-Order Correction). *Including the third-order term from Lemma 2.1, the expected entropy satisfies*

$$\mathbb{E}[H(\mathbf{p})] \approx H(\boldsymbol{\mu}) - \frac{1}{2} \sum_k \frac{\text{Var}[p_k]}{\mu_k} + \frac{1}{6} \sum_k \frac{m_{3,k}}{\mu_k^2}, \quad (11)$$

where $m_{3,k} = \mathbb{E}[(p_k - \mu_k)^3]$ is the third central moment, estimated as $\hat{m}_{3,k} = \frac{1}{S} \sum_{s=1}^S (p_k^{(s)} - \mu_k)^3$.

We use the third-order term as a *diagnostic* rather than a correction. Including it yields $C_k^{(3)} = \frac{1}{2} \text{Var}[p_k]/\mu_k - \frac{1}{6} m_{3,k}/\mu_k^2$, but the $1/\mu_k^2$ singularity can drive this quantity negative for right-skewed distributions near the simplex boundary, violating non-negativity (A0). More fundamentally, adding Taylor terms improves accuracy only when posterior samples are tightly concentrated around the mean, which is precisely not the high-uncertainty regime where the metric matters most. The skewness ratio ρ_k (Section 2.5) instead flags when the second-order approximation is unreliable, without compromising the guarantees of C_k .

Definition 2.10 (Skewness Diagnostic). For each class k with $\text{Var}[p_k] > 0$, define the reliability indicator

$$\rho_k(x) = \frac{|m_{3,k}|}{3 \mu_k \cdot \text{Var}[p_k]}. \quad (12)$$

To see why this is the right ratio, observe that the second-order contribution to MI from class k is $\frac{1}{2} \text{Var}[p_k]/\mu_k$, while the third-order correction is $\frac{1}{6} |m_{3,k}|/\mu_k^2$. Their ratio is

$$\frac{\frac{1}{6} |m_{3,k}|/\mu_k^2}{\frac{1}{2} \text{Var}[p_k]/\mu_k} = \frac{|m_{3,k}|}{3 \mu_k \cdot \text{Var}[p_k]} = \rho_k. \quad (13)$$

When $\rho_k \ll 1$, the third-order correction is negligible relative to C_k , and the approximation is reliable for class k . When ρ_k is appreciable (e.g., $\rho_k > 0.3$), the second-order approximation is degrading, and C_k should be interpreted with caution. The diagnostic is computable from the same S stochastic passes at negligible additional cost and can be reported alongside $C(x)$.

Off-diagonal structure and the CBEC metric. While $C(x)$ captures diagonal variance per class, the empirical covariance $\text{Cov}[\mathbf{p}]$ encodes complementary information about *pairwise confusion*. A strongly negative entry $\text{Cov}[p_i, p_j] \ll 0$ means that probability mass flows systematically between classes i and j across stochastic passes: the model is actively trading one for the other rather than being diffusely uncertain. In safety-critical settings this directional signal matters: a model torn between a safe and a critical class is qualitatively different from one torn between two safe classes, yet both can produce identical $\sum_k C_k$. When the skewness diagnostic (Section 2.5) flags unreliable C_k for rare critical classes ($\mu_k \approx 0$), we gate their product by the empirical negative correlation between safe and critical classes:

$$\text{CBEC}(x) = \sum_{i \in \mathcal{S}} \sum_{j \in \mathcal{C}} \sqrt{C_i \cdot C_j} \cdot \max(0, -\rho_{ij}), \quad (14)$$

where \mathcal{S} and \mathcal{C} are the safe and critical class sets and ρ_{ij} is the empirical Pearson correlation of p_i and p_j across the S forward passes. Three design choices interact. The *geometric mean* $\sqrt{C_i \cdot C_j}$ requires *both* classes to carry elevated epistemic uncertainty: single-class inflation is dampened by the square root, and if either class is certain the product vanishes. The *correlation gate* $\max(0, -\rho_{ij})$ filters coincidental co-elevation: the score is nonzero only when MC draws show the model actively exchanging probability between the two classes, a Taylor-free condition that remains reliable even when C_k degrades. The *restricted domain* $\mathcal{S} \times \mathcal{C}$ focuses the sum exclusively on cross-boundary confusion, excluding within-safe and within-critical co-elevation that carry no deferral signal. Together, these properties make CBEC the preferred fallback when $\rho_k > 0.3$ for critical classes; $C_{\text{crit_max}}$ remains the primary metric when the Taylor approximation is reliable.

3 SELECTIVE PREDICTION FOR DIABETIC RETINOPATHY

We evaluate $C(x)$ on selective prediction [Geifman and El-Yaniv, 2017] for diabetic retinopathy (DR) grading, a task where the cost of failure is acutely asymmetric: missing a sight-threatening retinopathy carries irreversible consequences, while a false positive triggers only a follow-up examination.

3.1 EXPERIMENTAL SETUP

Data. We pool three public DR grading benchmarks: EyePACS [Cuadros and Bresnick, 2009], APTOS 2019 [Asia Pacific Tele-Ophthalmology Society, 2019], and Messidor-2 [Decenci ere et al., 2014], totalling 39,970 colour fundus photographs. The International Clinical DR Severity Scale [Wilkinson et al., 2003] defines five grades; we consolidate the two most severe into a single grade because both

require urgent referral. The resulting four-class distribution places Grades 2–3 as *critical* ($\mathcal{C} = \{2, 3\}$, requiring treatment) and Grades 0–1 as *safe* ($\mathcal{S} = \{0, 1\}$); data are split patient-stratified into train/val/test with no patient leakage (full details in Appendix D.1).

Model. We construct a fully Bayesian EfficientNet-B4 [Tan and Le, 2019] using the low-rank variational inference framework of Toure and Stephens [2026], with a scale-mixture Gaussian prior ($\pi = 0.5$) and KL annealing. Full architectural details are in Appendix D.2.

Inference and evaluation. Uncertainty is estimated from $S = 30$ stochastic forward passes through the posterior. Our primary safety metric is the **critical false negative rate** (Critical FNR): among critical-class samples retained at a given coverage level, the fraction misclassified as safe. We summarise performance across coverage levels via the area under the selective risk curve (AUSC) [El-Yaniv and Wiener, 2010], with 95% CIs from 200 bootstrap resamples. On the test set, the Bayesian model achieves accuracy 0.8 and quadratic weighted kappa 0.65; per-class performance in Appendix D.3.

3.2 DEFERRAL POLICIES

We compare 10 deferral policies across four families (Table 1; formal definitions in Appendix C).

Table 1: Deferral policies evaluated. Higher score = defer. $\mathcal{C}=\{2, 3\}$, $\mathcal{S}=\{0, 1\}$.

Family	Policy	Score
Scalar	Entropy	$H[\bar{p}]$
	MI	$H[\bar{p}] - \mathbb{E}[H[p^{(t)}]]$
	MaxProb	$1 - \max_k \mu_k$
	Sale_EU_global	$\sum_k \sigma_k^2$
Per-class variance	Var_crit	$\max_{k \in \mathcal{C}} \sigma_k^2$
	Sale_EU_crit	$\sum_{k \in \mathcal{C}} \sigma_k^2$
Per-class MI	OvA_MI	$\sum_{k \in \mathcal{C}} \text{MI}_k^{\text{bin}}$
Per-class C_k (proposed)	$C_{\text{crit_sum}}$	$\sum_{k \in \mathcal{C}} C_k$
	$C_{\text{crit_max}}$	$\max_{k \in \mathcal{C}} C_k$
	CBEC	Eq. 14

Scalar baselines are class-agnostic; per-class variance targets critical classes via raw σ_k^2 but is confounded by μ_k (Lemma 2.4); OvA_MI computes binary MI per critical class. Our three proposed metrics build on $\sum_k C_k \approx \mathcal{I}$ (Section 2.2): $C_{\text{crit_max}}$ gives the sharpest signal when C_k estimates are reliable ($\rho_k < 0.3$); $C_{\text{crit_sum}}$ is a smoother alternative; CBEC (Eq. 14) gates safe–critical pairs by empirical negative correlation for robustness when skewness degrades C_k .

3.3 RESULTS

Theory validation. Before evaluating downstream performance, we verify the additive decomposition (8): $\sum_k C_k$ and exact MI achieve Pearson $r = 0.988$ and Spearman $r = 0.998$ across all 7,948 test samples (Figure 4), confirming the second-order approximation preserves epistemic uncertainty rankings. The skewness diagnostic (Section 2.5) shows C_k is reliable ($\rho_k < 0.3$) for >94% of safe-class samples and 82%/63% of Grade 2/3 respectively; full distributions in Appendix D.4.

Main results. Table 2 reports AUSC and Critical FNR at 80% coverage with bootstrap CIs. $C_{\text{crit_max}}$ achieves the lowest AUSC (0.285), reducing the area under the selective risk curve by 34.7% relative to MI (0.436, $p < 0.005$) and by 56.2% relative to Sale_EU_crit (0.650, $p < 0.005$). At the clinically relevant 80% coverage operating point, $C_{\text{crit_max}}$ achieves FNR 0.302, compared to 0.339 for MI and 0.409 for Sale_EU_crit.

Table 2: Selective prediction for DR grading (Bayesian EfficientNet-B4, $S=30$). AUSC integrates Critical FNR over all coverages (lower = safer). **Bold** = best; CIs: 200 bootstrap resamples.

Family	Policy	AUSC (Critical FNR)↓	Critical FNR @80%↓
Scalar	Entropy	0.604 ± 0.022	0.401 ± 0.016
	MI	0.436 ± 0.019	0.339 ± 0.014
	MaxProb	0.639 ± 0.022	0.439 ± 0.017
	Sale_EU_global	0.457 ± 0.018	0.341 ± 0.015
Per-class var.	Var_crit	0.606 ± 0.014	0.379 ± 0.016
	Sale_EU_crit	0.650 ± 0.013	0.409 ± 0.016
Per-class MI	OvA_MI	0.452 ± 0.017	0.367 ± 0.015
Per-class C_k (proposed)	$C_{\text{crit_sum}}$	0.327 ± 0.017	0.321 ± 0.014
	$C_{\text{crit_max}}$	0.285 ± 0.016	0.302 ± 0.013
	CBEC	0.416 ± 0.020	0.335 ± 0.014

Figure 1 visualises these results: $C_{\text{crit_max}}$ dominates across the full coverage range (left), with non-overlapping bootstrap interquartile ranges against scalar baselines (right).

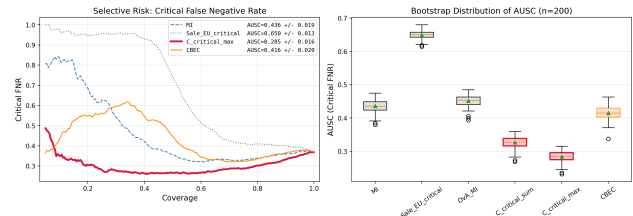


Figure 1: Selective prediction for DR. **Left:** Critical FNR vs. coverage; $C_{\text{crit_max}}$ dominates all baselines across the full range. **Right:** Bootstrap AUSC distribution ($n=200$); C_k -based policies (red/orange) show non-overlapping interquartile ranges against scalar baselines (grey).

The improvement over raw variance is especially striking. Sale_EU_crit and Var_crit (AUSC 0.650 and 0.606) perform *worse than entropy* (0.604), confirming that boundary

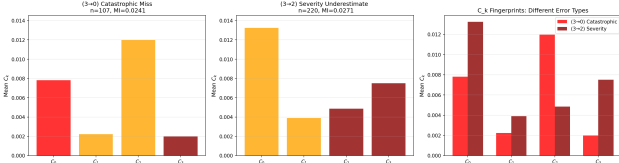


Figure 2: Epistemic signatures for Grade 3 errors with similar MI but distinct C_k patterns. **Left:** Catastrophic miss ($3 \rightarrow 0$, $MI=0.024$) concentrates on C_2 . **Centre:** Severity underestimate ($3 \rightarrow 2$, $MI=0.027$) elevates C_0 . **Right:** Grouped comparison showing the C_k fingerprints differ markedly despite similar MI, the catastrophic miss (red) peaks at C_2 while the severity error (dark red) peaks at C_0 .

suppression (Lemma 2.4) severely confounds unnormalised variance for critical classes with $\mu_k \approx 0.06$. The $1/\mu_k$ normalisation in C_k corrects precisely this: Grade 3 has mean probability ~ 0.06 , giving entropy curvature ~ 17 , so even small variance there carries large information-theoretic weight. This normalisation benefit is robust to the choice of inference method: a deep ensemble [Lakshminarayanan et al., 2017] of five members yields $C_{\text{crit_max}}$ AUSC 0.390 vs. 0.447 for Sale_EU_crit (12.9% reduction; Appendix D.12).

Interpretability: Error Signatures. A distinctive advantage of $\mathcal{C}(x)$ over scalar MI is that it reveals the *structure* of model confusion. Figure 2 shows that catastrophic misses (Grade 3 predicted as Grade 0) and severity underestimates (Grade 3 predicted as Grade 2) have nearly identical scalar MI (0.024 vs. 0.027 nats) but very different C_k signatures. The catastrophic miss concentrates epistemic mass on C_2 , identifying Grade 2 as the *bottleneck* of confusion, while the severity underestimate elevates C_0 , indicating doubt about healthy status. These qualitatively different failure modes, invisible to scalar metrics, suggest distinct remediation strategies; the epistemic confusion matrix (Appendix D.10) further confirms that cross-boundary confusion is $2.7\times$ stronger than within-group confusion, validating the clinical partition (detailed analysis in Appendix D.9).

MC dropout comparison. To test robustness to the posterior approximation, we repeat the evaluation using standard MC dropout [Gal and Ghahramani, 2016] ($p=0.3$, $S=30$). The ranking changes markedly: CBEC achieves the lowest AUSC (0.197 ± 0.012 , winning 100% of bootstrap samples), a 53.6% reduction over MI (0.425 ± 0.024), while $C_{\text{crit_max}}$ drops to 0.419. MC dropout is known to produce regions of spurious confidence where the approximate posterior underestimates uncertainty [Smith and Gal, 2018]. In our framework, this inflates ρ_k for critical classes, degrading the Taylor approximation underlying C_k while leaving CBEC’s correlation gate intact. This confirms the intended complementarity: $C_{\text{crit_max}}$ is the primary metric under well-calibrated posteriors; CBEC provides a robust fallback

when ρ_k signals degradation. Full results in Appendix D.11.

4 OUT-OF-DISTRIBUTION DETECTION

We evaluate the per-class epistemic uncertainty metric on out-of-distribution (OoD) detection, where elevated epistemic uncertainty should signal distributional shift.

4.1 SETUP

Datasets. We consider two OoD detection tasks spanning different modalities and class structures.

FashionMNIST [Xiao et al., 2017] \rightarrow KM-NIST [Clanuwat et al., 2018]: A 10-class image classification task where the model is trained on FashionMNIST (50,000 train, 10,000 test) and evaluated on KMNIST (10,000 samples) as OoD.

MIMIC-III ICU [Johnson et al., 2016] \rightarrow Newborn: A binary mortality prediction task on tabular clinical data (44 features) where the model is trained on adult ICU admissions (40,406 train, 4,490 test) and evaluated on the Newborn unit (5,357 samples) as OoD.

Model. Both tasks use low-rank Bayesian neural networks with Gaussian posteriors. FashionMNIST: two hidden layers (1200 units, rank 25), $S=50$ MC samples. MIMIC-III: two hidden layers (128 units, rank 15), $S=512$ MC samples, with class-weighted training to address mortality imbalance (8.6% prevalence). See Appendix E.2 for full architectural and training details.

Metrics. We compare four uncertainty scores: negative maximum softmax probability [Hendrycks and Gimpel, 2017], MI, $EU_{\text{var}} = \sum_k \sigma_k^2$, and our proposed $\sum_k C_k$. Performance is measured by AUROC (ID samples labelled 0, OoD samples labelled 1); results are mean \pm std over 5 seeds.

4.2 RESULTS

Table 3 summarises OoD detection performance. $\sum_k C_k$ achieves the highest AUROC on both datasets: 0.735 ± 0.009 on FashionMNIST versus 0.724 for MI, and 0.815 ± 0.017 on MIMIC-III versus 0.802 for MI. The OoD-to-ID ratio column reveals the mechanism: on FashionMNIST, $\sum_k C_k$ amplifies the distributional shift signal to $6.43\times$ versus $5.92\times$ for MI. On FashionMNIST, this effect is predicted by Lemma 2.9: the gap $\sum_k C_k - MI \approx \frac{1}{6} \sum_k m_{3,k} / \mu_k^2$ grows with posterior skewness, and OoD samples produce higher skewness diagnostic ρ_k than ID samples across all ten classes (Appendix E.6, Figure 14). On MIMIC-III the picture is more nuanced: the survival class ($k=0$) follows the expected pattern ($\rho_0^{\text{OOD}} > \rho_0^{\text{ID}}$, median shift +43%), but

Table 3: OoD detection: AUROC and OoD/ID mean-uncertainty ratio. Best in **bold**.

Family	Method	FashionMNIST \rightarrow KMNIST		MIMIC-III ICU \rightarrow Newborn	
		AUROC \uparrow	Ratio \uparrow	AUROC \uparrow	Ratio \uparrow
Baselines	Neg. MSP	0.665 \pm 0.013	2.07	0.688 \pm 0.030	1.24
	MI	0.724 \pm 0.009	5.92	0.802 \pm 0.004	1.61
	EU_{var}	0.710 \pm 0.010	5.92	0.778 \pm 0.015	1.71
Proposed	$\sum_k C_k$	0.735 \pm 0.009	6.43	0.815 \pm 0.017	1.62

the mortality class ($k=1$) reverses because near-zero μ_1 for newborns collapses $\text{Var}[p_1]$ faster than $1/\mu_1$ can compensate, concentrating the third-order signal entirely in class 0 (Appendix E.6).

The unnormalised baseline EU_{var} underperforms MI on both datasets despite matching its ratio on FashionMNIST ($5.92\times$): without mean-normalisation, raw variance σ_k^2 is bounded above by $\mu_k(1 - \mu_k)$, compressing the dynamic range of uncertainty scores. Strikingly, on MIMIC-III EU_{var} achieves the *highest* ratio ($1.71\times$) yet the *lowest* AUROC among epistemic measures. A high mean ratio does not imply good separability: AUROC depends on the full distributional overlap, and the un-normalised variance sum concentrates both ID and OoD scores near zero with a shared heavy tail, so the numerically large mean shift is swamped by within-group spread (Appendix E.5, Figure 12). This pattern is consistent across inference methods: a deep ensemble replicates the same ranking ($\sum_k C_k=0.753 > \text{MI}=0.752 > EU_{\text{var}}=0.750$) on MIMIC-III, with EU_{var} again achieving the highest ratio ($2.72\times$) and the lowest AUROC (Appendix E.7).

Per-class decomposition. On the binary MIMIC-III task, the decomposition $\sum_k C_k = C_0 + C_1$ reveals that distributional shift affects the two classes asymmetrically ($2.03\times$ for survival vs. $1.30\times$ for mortality): the larger OoD signal resides in the *non-critical* class, so C_1 -only yields AUROC 0.740, well below $\sum_k C_k$ at 0.815. On FashionMNIST the pattern is the opposite: all ten per-class C_k values increase uniformly from ID to OoD (Appendix E.4, Figure 11), consistent with KMNIST inducing a structural rather than semantic shift that does not concentrate on any subset of classes. Together, these two cases illustrate a task-dependent trade-off: critical-class targeting improves selective prediction (Section 3) but all-class aggregation is necessary for OoD detection, where the locus of distributional shift is not known a priori and can be either asymmetric (MIMIC-III) or uniform (FashionMNIST). Full per-class results in Appendix E.3.

5 EPISTEMIC SENSITIVITY TO DATA QUALITY

We assess whether $\sum_k C_k$ remains insensitive to irreducible aleatoric noise under controlled label-noise injection.

5.1 SETUP

Data. We use Fashion-MNIST ($K=10$, 60,000 images) and CIFAR-10 ($K=10$, 50,000 images). For each dataset we inject symmetric label noise at rates $\alpha \in \{0.1, 0.2, 0.3, 0.4, 0.5\}$: a fraction α of training labels is replaced uniformly at random, increasing aleatoric uncertainty without altering the input distribution.

Model. Both tasks use fully Bayesian networks trained end-to-end from scratch with low-rank Gaussian posteriors. Fashion-MNIST: two hidden layers (400 units, rank 15), $S=50$ MC samples. CIFAR-10: Conv $32 \rightarrow 64 \rightarrow 128$ with global average pooling and a low-rank Bayesian head (rank 32), $S=50$ MC samples. Full architectural details are in Appendix F.1.

Protocol. For each noise level α we compute the mean aleatoric uncertainty $\bar{U}_a(\alpha) = \frac{1}{N} \sum_i \mathbb{E}[H(\mathbf{p}_i)]$ and the mean epistemic uncertainty $\bar{U}_e(\alpha)$ using either MI or $\sum_k C_k$ over the clean test set. The relative disentanglement ratio

$$R_{\text{rel}}(\alpha) = \frac{(\bar{U}_e(\alpha) - \bar{U}_e(0)) / \bar{U}_e(0)}{(\bar{U}_a(\alpha) - \bar{U}_a(0)) / \bar{U}_a(0)} \quad (15)$$

measures the percentage increase in epistemic uncertainty per percentage increase in aleatoric uncertainty. $R_{\text{rel}} = 0$ indicates perfect disentanglement; $R_{\text{rel}} = 1$ indicates full entanglement; values above 0.3 signal substantial contamination (see Appendix F.2 for the motivation behind the relative formulation over the absolute ratio).

5.2 RESULTS

Table 4 reports $|R_{\text{rel}}|$ for low-rank Bayesian models under three configurations. Under end-to-end training, both metrics are near-perfectly disentangled ($|R_{\text{rel}}| \ll 0.3$ everywhere), confirming that end-to-end Bayesian training with low-rank posteriors is the regime that produces the least entangled uncertainty estimates. It is also the regime under which the second-order Taylor expansion most accurately approximates exact MI: at $\alpha=0$, $\sum_k C_k / \text{MI}$ is $1.00\times$ on Fashion-MNIST and $1.02\times$ on CIFAR-10 (Table 22). $\sum_k C_k$ achieves lower $|R_{\text{rel}}|$ in 9 of the 10 end-to-end conditions, the exception being CIFAR-10 at $\alpha=0.1$ where both values remain below 0.05. The rightmost block contrasts the *same model type and dataset* (CIFAR-10, low-rank) under transfer learning: ratios jump to 0.74–1.97, an order-of-magnitude degradation that isolates the training regime as the causal factor.

The posterior approximation matters as much as the metric. The transfer-learning column in Table 4 already isolates training regime as a causal factor; within a single regime the posterior family matters too. On Fashion-MNIST, where all three model types are trained end-to-

Table 4: $|R_{\text{rel}}(\alpha)|$ for low-rank Bayesian models. Lower is better; $\dagger = \sum_k C_k$ less entangled. The first two blocks use end-to-end training (e2e); the third uses a frozen ResNet-50 backbone with a low-rank Bayesian head (TL).

α	FMNIST (e2e)		CIFAR-10 (e2e)		CIFAR-10 (TL)	
	MI	$\sum_k C_k$	MI	$\sum_k C_k$	MI	$\sum_k C_k$
0.1	0.023	0.005 [†]	0.040	0.047	1.830	1.970
0.2	0.010	0.003 [†]	0.012	0.007 [†]	1.344	1.435
0.3	0.008	0.002 [†]	0.009	0.004 [†]	0.991	1.039
0.4	0.005	0.003 [†]	0.020	0.016 [†]	0.832	0.868
0.5	0.009	0.002 [†]	0.020	0.017 [†]	0.737	0.760

end, the low-rank model achieves a mean $|R_{\text{rel}}|$ below 0.01 for both metrics, while the full-rank model reaches 0.11 (MI)/0.10 ($\sum_k C_k$) and MC dropout 0.10/0.06 respectively (Appendix F.2). Under transfer learning the ordering is preserved across both CIFAR-10 and CIFAR-100: low-rank < full-rank < MC dropout, with MC dropout ratios exceeding 0.58 on CIFAR-100 at $\alpha=0.1$. This suggests that the high entanglement reported by Mucsányi et al. [2024] reflects not only limitations of the decomposition formula but also the quality of the underlying posterior approximation: models that do not propagate uncertainty through the full network produce predictive distributions whose variance structure is poorly suited to any epistemic measure, whether MI or $\sum_k C_k$. Across all end-to-end configurations (Figure 15), $\sum_k C_k$ achieves lower $|R_{\text{rel}}|$ than MI in 19 of 20 conditions (4 models \times 5 noise levels). Under transfer learning the advantage is partial, with MI prevailing where baseline inflation $\sum_k C_k / \text{MI}$ exceeds $1.6 \times$ (Table 22), i.e. precisely where the Taylor approximation is least accurate. Full transfer-learning results and an analysis of the rank constraint’s effect on uncertainty scale are in Appendix F.2.

Sensitivity to class cardinality. On CIFAR-100, the $1/\mu_k$ normalisation amplifies contributions from low-probability classes, inflating $\sum_k C_k$ relative to MI by $1.17 \times$ for the low-rank model and $1.89 \times$ for MC dropout. The $\mathcal{O}(K^2)$ scaling analysis and mitigation strategies are detailed in Appendix F.3.

6 DISCUSSION AND CONCLUSION

We presented a per-class epistemic uncertainty decomposition $C(x)$ derived from a second-order Taylor expansion of MI, where the $1/\mu_k$ normalisation arises naturally from the entropy Hessian and counteracts boundary suppression. The decomposition reduces to a simple ratio of variance to mean per class, adds negligible cost to any posterior sampling pipeline, and recovers scalar MI by summation.

The three experiments exposed a consistent theme: the value of $C(x)$ lies not in being a better scalar summary but in

enabling class-specific queries that scalar metrics cannot express. For selective prediction, targeting critical-class C_k outperformed all scalar and variance-based baselines; for OoD detection, the per-class view revealed that distributional shift can concentrate asymmetrically across classes, a structure invisible to any aggregate score; for disentanglement, the decomposition provided a lens to diagnose when and why epistemic and aleatoric signals become entangled.

A finding we did not anticipate is that the posterior approximation shaped metric behaviour at least as strongly as the metric itself. Switching from variational inference to MC dropout reversed the ranking of our deferral policies, because dropout inflated skewness precisely for the rare classes where the Taylor expansion is most sensitive. The disentanglement experiments sharpened this further: freezing a pretrained backbone and attaching a Bayesian head degraded AU/EU separation by over an order of magnitude compared to end-to-end training, even when the Bayesian component was identical. This raises a question for the growing literature on post-hoc Bayesian methods: if features are learned without any posterior objective, the resulting variance structure may not support meaningful epistemic attribution regardless of the last-layer treatment. We do not suggest post-hoc methods lack practical value, but the quality of their uncertainty outputs deserves scrutiny commensurate with the attention given to their scalability.

Several limitations exist. The additive link $\sum_k C_k \approx \mathcal{I}$ loosens under high skewness over low-probability classes, since the third-order remainder scales as $1/\mu_k^2$; ρ_k diagnoses but does not correct this, and the CBEC fallback requires domain knowledge to define class partitions. The $1/\mu_k$ normalisation introduces $\mathcal{O}(K^2)$ scaling of the aggregate, necessitating truncation or reweighting in high-cardinality settings, though the per-class vector itself remains fully interpretable. All models use MFVI, low-rank Gaussian VI, MC dropout or deep ensembles. Characterising how C_k behaves under other approximate inference schemes such as Laplace approximations [Daxberger et al., 2021] or stochastic weight averaging [Maddox et al., 2019] is a natural next step.

The decomposition is not tied to any specific posterior family or architecture. Future work includes extending $C(x)$ to structured prediction tasks where class identity is less cleanly defined, integrating it into active learning acquisition functions that target specific classes, and combining low-rank ensembles with per-class attribution for richer uncertainty profiles. More fundamentally, making end-to-end Bayesian training more practical strikes us as a more promising path than refining post-hoc corrections, and the per-class decomposition is designed to complement that direction.⁴

⁴Code and trained models are available in the supplementary material.

References

- Asia Pacific Tele-Ophthalmology Society. APTOS 2019 blindness detection. Kaggle Competition, 2019. URL <https://www.kaggle.com/c/aptos2019-blindness-detection>.
- Zeynep Sonat Baltaci, Kemal Oksuz, Selim Kuzucu, Kivanc Tezoren, Berkin Kerim Konar, Alpay Ozkan, Emre Akbas, and Sinan Kalkan. Class uncertainty: A measure to mitigate class imbalance. *arXiv preprint arXiv:2311.14090*, 2023.
- David M Blei, Alp Kucukelbir, and Jon D McAuliffe. Variational inference: A review for statisticians. *Journal of the American statistical Association*, 112(518):859–877, 2017.
- Charles Blundell, Julien Cornebise, Koray Kavukcuoglu, and Daan Wierstra. Weight uncertainty in neural networks. In *Proceedings of the 32nd International Conference on Machine Learning (ICML)*, pages 1613–1622. PMLR, 2015.
- Robin Camarasa, Daniel Bos, Jeroen Hendrikse, Paul Nederkoorn, M. Eline Kooi, Aad van der Lugt, and Marleen de Bruijne. A quantitative comparison of epistemic uncertainty maps applied to multi-class segmentation. *Machine Learning for Biomedical Imaging*, 1(UNSURE2020): 1–39, September 2021. ISSN 2766-905X. doi: 10.59275/j.melba.2021-ec49. URL <http://dx.doi.org/10.59275/j.melba.2021-ec49>.
- Tarin Clanuwat, Mikel Bober-Irizar, Asanobu Kitamoto, Alex Lamb, Kazuaki Yamamoto, and David Ha. Deep learning for classical japanese literature. *arXiv preprint arXiv:1812.01718*, 2018.
- David R. Cox and Peter A. W. Lewis. *The Statistical Analysis of Series of Events*. Methuen, London, 1966.
- Jorge Cuadros and George Bresnick. Eyepacs: an adaptable telemedicine system for diabetic retinopathy screening. *Journal of diabetes science and technology*, 3(3):509–516, 2009.
- Erik Daxberger, Agustinus Kristiadi, Alexander Immer, Runa Eschenhagen, Matthias Bauer, and Philipp Henning. Laplace redux—effortless bayesian deep learning. In *Proceedings of the 35th International Conference on Neural Information Processing Systems*, pages 20089–20103, 2021.
- Ivo Pascal de Jong, Andreea Ioana Sburlea, Matthia Sabatelli, and Matias Valdenegro-Toro. Measuring orthogonality as the blind-spot of uncertainty disentanglement, 2026. URL <https://arxiv.org/abs/2408.12175>.
- Etienne Decencière, Xiwei Zhang, Guy Cazuguel, Bruno Lay, Béatrice Cochener, Caroline Trone, Philippe Gain, John-Richard Ordóñez-Varela, Pascale Massin, Ali Erginay, et al. Feedback on a publicly distributed image database: the messidor database. *Image Analysis & Stereology*, pages 231–234, 2014.
- Stefan Depeweg, Jose-Miguel Hernandez-Lobato, Finale Doshi-Velez, and Steffen Udluft. Decomposition of uncertainty in bayesian deep learning for efficient and risk-sensitive learning. In *International conference on machine learning*, pages 1184–1193. PMLR, 2018.
- Ruxiao Duan, Brian Caffo, Harrison X. Bai, Haris I. Sair, and Craig Jones. Evidential uncertainty quantification: A variance-based perspective. In *Proceedings of the IEEE/CVF Winter Conference on Applications of Computer Vision (WACV)*, pages 2132–2141, 2024.
- Ran El-Yaniv and Yair Wiener. On the foundations of noise-free selective classification. *JMLR*, 11:1605–1641, 2010.
- Ugo Fano. Ionization yield of radiations. II. The fluctuations of the number of ions. *Physical Review*, 72(1):26–29, 1947.
- Yarin Gal and Zoubin Ghahramani. Dropout as a Bayesian approximation: Representing model uncertainty in deep learning. In *Proceedings of the 33rd International Conference on Machine Learning (ICML)*, pages 1050–1059. PMLR, 2016.
- Yarin Gal, Riashat Islam, and Zoubin Ghahramani. Deep Bayesian active learning with image data. In *International conference on machine learning*, pages 1183–1192. PMLR, 2017.
- Yonatan Geifman and Ran El-Yaniv. Selective classification for deep neural networks. In *Advances in Neural Information Processing Systems (NeurIPS)*, volume 30, 2017.
- Fredrik K. Gustafsson, Martin Danelljan, and Thomas B. Schön. Evaluating scalable Bayesian deep learning methods for robust computer vision. In *Proceedings of the IEEE/CVF Conference on Computer Vision and Pattern Recognition Workshops (CVPRW)*, pages 318–319, 2020.
- Dan Hendrycks and Kevin Gimpel. A baseline for detecting misclassified and out-of-distribution examples in neural networks. In *International Conference on Learning Representations (ICLR)*, 2017.
- Neil Houlsby, Ferenc Huszár, Zoubin Ghahramani, and Máté Lengyel. Bayesian active learning for classification and preference learning. *arXiv preprint arXiv:1112.5745*, 2011.

- Alistair E. W. Johnson, Tom J. Pollard, Lu Shen, Li-wei H. Lehman, Mengling Feng, Mohammad Ghassemi, Benjamin Moody, Peter Szolovits, Leo Anthony Celi, and Roger G. Mark. MIMIC-III, a freely accessible critical care database. *Scientific Data*, 3(1):160035, 2016.
- Alex Kendall and Yarin Gal. What uncertainties do we need in Bayesian deep learning for computer vision? In *Advances in Neural Information Processing Systems (NeurIPS)*, volume 30, pages 5574–5584, 2017.
- Salman Khan, Munawar Hayat, Syed Waqas Zamir, Jianbing Shen, and Ling Shao. Striking the right balance with uncertainty. In *Proceedings of the IEEE/CVF Conference on Computer Vision and Pattern Recognition*, pages 103–112, 2019.
- Balaji Lakshminarayanan, Alexander Pritzel, and Charles Blundell. Simple and scalable predictive uncertainty estimation using deep ensembles. In *Advances in Neural Information Processing Systems (NeurIPS)*, volume 30, 2017.
- Wesley J Maddox, Timur Garipov, Pavel Izmailov, Dmitry Vetrov, and Andrew Gordon Wilson. A simple baseline for bayesian uncertainty in deep learning. In *Proceedings of the 33rd International Conference on Neural Information Processing Systems*, pages 13153–13164, 2019.
- Andrey Malinin and Mark Gales. Predictive uncertainty estimation via prior networks. In S. Bengio, H. Wallach, H. Larochelle, K. Grauman, N. Cesa-Bianchi, and R. Garnett, editors, *Advances in Neural Information Processing Systems*, volume 31. Curran Associates, Inc., 2018. URL https://proceedings.neurips.cc/paper_files/paper/2018/file/3ea2db50e62ceefceaf70a9d9a56a6f4-Paper.pdf.
- Bálint Mucsányi, Michael Kirchhof, and Seong Joon Oh. Benchmarking uncertainty disentanglement: specialized uncertainties for specialized tasks. In *Proceedings of the 38th International Conference on Neural Information Processing Systems*, pages 50972–51038, 2024.
- Yusuf Sale, Paul Hofman, Timo Löhr, Lisa Wimmer, Thomas Nagler, and Eyke Hüllermeier. Label-wise aleatoric and epistemic uncertainty quantification. In *Proceedings of the 40th Conference on Uncertainty in Artificial Intelligence (UAI)*, volume 244 of *Proceedings of Machine Learning Research*, pages 3159–3179. PMLR, 2024.
- Murat Sensoy, Lance Kaplan, and Melih Kandemir. Evidential deep learning to quantify classification uncertainty. In S. Bengio, H. Wallach, H. Larochelle, K. Grauman, N. Cesa-Bianchi, and R. Garnett, editors, *Advances in Neural Information Processing Systems*, volume 31. Curran Associates, Inc., 2018. URL https://proceedings.neurips.cc/paper_files/paper/2018/file/a981f2b708044d6fb4a71a1463242520-Paper.pdf.
- Lewis Smith and Yarin Gal. Understanding measures of uncertainty for adversarial example detection. In *Proceedings of the 34th Conference on Uncertainty in Artificial Intelligence (UAI)*, pages 560–569, 2018.
- Mingxing Tan and Quoc V. Le. EfficientNet: Rethinking model scaling for convolutional neural networks. In *Proceedings of the 36th International Conference on Machine Learning (ICML)*, pages 6105–6114. PMLR, 2019.
- Mame Diarra Toure and David A Stephens. Singular bayesian neural networks. *arXiv preprint arXiv:2602.00387*, 2026.
- Richard Eric Turner and Maneesh Sahani. *Two problems with variational expectation maximisation for time series models*, page 104–124. Cambridge University Press, 2011.
- Charles P Wilkinson, Frederick L Ferris III, Ronald E Klein, Paul P Lee, Carl David Agardh, Matthew Davis, Diana Dills, Anselm Kampik, Rangasamy Pararajasegaram, Juan T Verdaguer, et al. Proposed international clinical diabetic retinopathy and diabetic macular edema disease severity scales. *Ophthalmology*, 110(9):1677–1682, 2003.
- Lisa Wimmer, Yusuf Sale, Paul Hofman, Bernd Bischl, and Eyke Hüllermeier. Quantifying aleatoric and epistemic uncertainty in machine learning: Are conditional entropy and mutual information appropriate measures? In *Proceedings of the 39th Conference on Uncertainty in Artificial Intelligence (UAI)*, volume 216 of *Proceedings of Machine Learning Research*, pages 2282–2292. PMLR, 2023.
- Han Xiao, Kashif Rasul, and Roland Vollgraf. Fashion-mnist: a novel image dataset for benchmarking machine learning algorithms. *arXiv preprint arXiv:1708.07747*, 2017.

Not Just How Much, But Where: Decomposing Epistemic Uncertainty into Per-Class Contributions (Supplementary Material)

Mame Diarra Toure¹

David A. Stephens¹

¹Department of Mathematics and Statistics , McGill University

A BACKGROUND AND RELATED WORK

This appendix provides the detailed literature context that supports the compressed survey in the main text. We organise the discussion into four parts: (i) the axiomatic framework and the label-wise variance approach; (ii) evidential and Dirichlet-based per-class uncertainty; (iii) class-imbalance and multi-class segmentation perspectives; and (iv) AU/EU disentanglement, scalar epistemic baselines, and the orthogonality criterion.

A.1 AXIOMATIC FRAMEWORK AND THE LABEL-WISE APPROACH

Wimmer et al. (2023) – Axioms for epistemic uncertainty. Wimmer et al. [2023] formalise a set of axioms A0–A5 for second-order uncertainty measures in K -class classification. An uncertainty measure is defined over a *second-order distribution* $Q \in \Delta_K^{(2)}$, a distribution over probability simplices $p \in \Delta^K$, with mean $\mu = \mathbb{E}_Q[p]$. The five axioms relevant to our analysis are:

- **A0** (Non-negativity): $\text{EU}(Q) \geq 0$.
- **A1** (Vanishing at certainty): $\text{EU}(Q) = 0$ if and only if $Q = \delta_\theta$ for some $\theta \in \Delta^K$.
- **A2** (Maximum at uniform): EU is maximised when Q is the uniform distribution on Δ^K .
- **A3** (Monotone under mean-preserving spread): if Q' is a mean-preserving spread of Q (i.e. Q' has the same mean but weakly larger variance in every direction), then $\text{EU}(Q') \geq \text{EU}(Q)$.
- **A5** (Location-shift invariance): a spread-preserving shift of Q 's mean along the simplex does not change $\text{EU}(Q)$.

Wimmer et al. show that mutual information satisfies A0 and A1, but violates A2 (their Proposition 2), A3 (Proposition 4; a counterexample exists already for $K=2$), and A5 (Proposition 3). No single measure simultaneously satisfies all five axioms. Our aggregate $\sum_k C_k$ satisfies A0, A1, and A3 but violates A2 and A5; as Corollary 2.7 establishes, the A5 violation is the *precise mechanism* that corrects boundary suppression.

Sale et al. (2024) – Label-wise decomposition. Sale et al. [2024] introduce a label-wise framework that reduces a K -class problem to K binary sub-problems via one-vs-rest binarisation. For each class k , the true class probability Θ_k is treated as a scalar random variable following a second-order distribution Q_k (capturing model uncertainty over possible probability values for class k). Per-class total, aleatoric, and epistemic uncertainty are defined via proper scoring rules; under squared loss the epistemic measure is

$$\text{EU}_k = \text{Var}(\Theta_k), \quad (16)$$

and the global quantities are sums: $\text{EU} = \sum_k \text{Var}(\Theta_k)$. Sale et al. prove (their Theorem 3.2) that these variance-based measures satisfy axioms A0, A1, A3 (strict version), A4 (strict version), A5, A6, and A7, a stronger axiomatic profile than entropy-based measures, which fail A5 [Wimmer et al., 2023].

Two limitations motivate our normalised alternative. First, *boundary suppression*: because $p_k \in [0, 1]$, the constraint $\text{Var}[p_k] \leq \mu_k(1 - \mu_k)$ (Lemma 2.4) forces $\text{EU}_k \rightarrow 0$ as $\mu_k \rightarrow 0$, regardless of how strongly the stochastic forward passes disagree. This “edge-squeeze” masks epistemic uncertainty for precisely the rare, low-base-rate classes where it matters most, rendering EU_k incomparable across classes with different mean probabilities. Second, the framework operates on marginals Q_k in isolation; consequently, the global sum $\sum_k H(\bar{\theta}_k)$ does not recover the standard multiclass mutual information decomposition, preventing direct additive attribution of MI to individual classes. Our C_k addresses both limitations: the $1/\mu_k$ normalisation removes the base-rate confound, and by construction $\sum_k C_k \approx \mathcal{I}$ (Section 2.2).

A.2 EVIDENTIAL AND DIRICHLET-BASED PER-CLASS UNCERTAINTY

Sensoy et al. (2018) and Malinin & Gales (2018). Sensoy et al. [2018] propose Evidential Deep Learning (EDL), training a neural network to output Dirichlet concentration parameters $\alpha = (\alpha_1, \dots, \alpha_K)$ in a single forward pass, thereby placing a distribution directly over the simplex. Malinin and Gales [2018] independently introduced Prior Networks with the same Dirichlet parameterisation but a different training objective (reverse KL from a target Dirichlet), and formalised the decomposition of predictive uncertainty into distributional uncertainty (epistemic) and data uncertainty (aleatoric) within this framework. Both approaches provide per-class quantities derived from the Dirichlet parameters without requiring multiple stochastic forward passes.

Duan et al. (2024). Duan et al. [2024] extend the evidential paradigm by applying the law of total covariance to the Dirichlet-Categorical hierarchy. For a Dirichlet with concentration α and strength $\alpha_0 = \sum_k \alpha_k$, they derive the full per-class epistemic covariance matrix (their Equation 21)

$$\text{Cov}_{c,c'}^{\text{epis}} = \frac{1}{\alpha_0 + 1} (\bar{\mu}_c \mathbf{1}_{c=c'} - \bar{\mu}_c \bar{\mu}_{c'}), \quad (17)$$

whose diagonal gives the per-class epistemic variance (Equation 24) $U_c^{\text{epis}} = \frac{1}{\alpha_0 + 1} \bar{\mu}_c (1 - \bar{\mu}_c)$, and whose off-diagonal entries reveal pairwise class confusion. The covariance structure therefore carries both marginal and joint epistemic information in closed form.

However, the entire covariance matrix is determined solely by $\bar{\mu} = \alpha/\alpha_0$ and the scalar strength α_0 . This means that two inputs with the same Dirichlet mean but very different patterns of stochastic-forward-pass disagreement will receive identical epistemic covariance matrices, a rigidity absent from empirical MC-based estimates. More fundamentally, placing a Dirichlet prior on the simplex is a strong distributional assumption: the Dirichlet family is conjugate and analytically convenient, but real posterior predictive distributions under deep networks are rarely Dirichlet-shaped. Our approach makes no distributional assumption and recovers class-confusion information from the empirical covariance $\widehat{\text{Cov}}[\mathbf{p}]$ computed directly from MC samples.

A.3 CLASS IMBALANCE AND MULTI-CLASS SEGMENTATION

Khan et al. (2019). Khan et al. [2019] demonstrate that MC-dropout predictive uncertainty (computed as the second moment of the softmax output across dropout masks, following Gal and Ghahramani 2016) correlates with both the rarity of classes and the difficulty of individual samples. They exploit this correlation to reshape classification margins: rare, high-uncertainty classes receive larger margin penalties, improving generalisation for under-represented classes across face verification, attribute prediction, and classification tasks. Importantly, the uncertainty used is the total predictive uncertainty (the combined effect of aleatoric and epistemic sources via the MC-dropout second moment); no explicit AU/EU decomposition is performed, and the uncertainty is used as a *class-level signal* derived from the training set rather than an input-level epistemic vector.

Baltaci et al. (2023). Baltaci et al. [2023] propose Class Uncertainty (CU), defined as the average predictive entropy across training examples within each class:

$$\tilde{\mu}_c^U = \frac{1}{N_c} \sum_{i=1}^{N_c} u^{(i)}, \quad u^{(i)} = - \sum_{c' \in \mathcal{C}} \bar{p}_{c'}^{(i)} \log \bar{p}_{c'}^{(i)}, \quad (18)$$

where $\bar{p}_{c'}^{(i)}$ is the ensemble-averaged class probability for sample i (their Equations 8–9); a normalised version $\mu_c^U = \tilde{\mu}_c^U / \sum_{c'} \tilde{\mu}_{c'}^U$ is then used as the class-imbalance weight (Equation 10). CU captures *semantic imbalance*, difficulty differ-

ences among classes that go beyond mere class cardinality, and is shown to correlate more strongly with class-wise test error than cardinality alone (Spearman $\rho = 0.92$ vs. 0.82).

CU has two limitations relative to our goal. First, it is a *dataset-level aggregate*: it aggregates over training examples and is not defined for a single test input, so it cannot provide input-level epistemic attribution. Second, it uses predictive entropy, which conflates aleatoric and epistemic components; no decomposition into EU and AU is performed.

Camarasa et al. (2021). Camarasa et al. [2021] provide a systematic quantitative comparison of epistemic uncertainty metrics in multi-class carotid artery MR segmentation, evaluating one-vs-all entropy, mutual information, and class-wise variance maps across both combined and class-specific settings. Their key empirical finding is that raw class-wise variance underperforms one-vs-all entropy in the class-specific setting (where it decorrelates from misclassification rate), while entropy-based metrics maintain stronger correlation with segmentation errors across all classes. Lemma 2.4 establishes this as a mathematical inevitability rather than a dataset artefact: variance is structurally suppressed near the simplex boundary regardless of actual posterior disagreement, making it an unreliable epistemic signal precisely where the information would be most valuable.

A.4 AU/EU DISENTANGLEMENT, SCALAR BASELINES, AND THE ORTHOGONALITY CRITERION

Smith & Gal (2018) – Taylor connection and MC-dropout failure modes. Smith and Gal [2018] analyse the relationship between softmax variance and mutual information through a Taylor expansion of the logarithm. They show (their Equation 10, Section 3.2) that the leading term in the MI series is exactly proportional to the mean variance across classes:

$$\hat{I} = \sum_j \left(\frac{1}{T} \sum_i p_{ij}^2 \right) - \hat{p}_j^2 + \mathcal{O}(\text{higher order}), \quad (19)$$

which is, up to a multiplicative constant, the mean variance score $\hat{\sigma}^2 = \frac{1}{C} \sum_j \text{Var}[p_j]$. This provides a theoretical explanation for why variance-based uncertainty estimates empirically approximate MI and underscores the Taylor-expansion approach underlying our C_k decomposition; the key difference is that our expansion is applied *per class* rather than averaged, yielding class-level attribution.

Smith & Gal also document failure modes of MC-dropout: the approximate posterior tends to underestimate uncertainty and can produce spuriously confident regions in latent space where the model assigns high confidence to inputs far from any training data. We observe this behaviour in the DR experiment (Section 3): under MC-dropout, the skewness diagnostic ρ_k is elevated for critical (rare) classes, degrading the C_k Taylor approximation and causing $C_{\text{crit_max}}$ to underperform its BNN counterpart.

Houlsby et al. (2011) – BALD and scalar epistemic uncertainty. Houlsby et al. [2011] introduce Bayesian Active Learning by Disagreement (BALD), originally for Gaussian processes and binary classifiers, selecting data points that maximise the mutual information $\mathcal{I}(y; \omega \mid x)$ between labels and model parameters; this objective was subsequently adopted as the canonical scalar epistemic measure in Bayesian deep learning [Gal et al., 2017]. BALD demonstrated its power for reducing posterior uncertainty in active learning. However, MI is class-agnostic: a high MI value signals that *some* class confusion is driving uncertainty, but does not identify *which* classes are the locus of the model’s ignorance. Our C_k vector decomposes MI into per-class contributions, preserving the additive structure of the BALD objective while exposing the class-level anatomy of epistemic uncertainty.

Hendrycks & Gimpel (2017) – Maximum softmax probability. Hendrycks and Gimpel [2017] demonstrate that the maximum softmax probability (MSP), $\max_k \mu_k$, provides a surprisingly effective baseline for detecting both misclassified and out-of-distribution examples, despite the fact that softmax probabilities are known to be poorly calibrated as direct confidence estimates in deep networks. We include the complementary uncertainty score $1 - \text{MSP} = 1 - \max_k \mu_k$ as a scalar baseline in our deferral policy comparison (Table 1). This score is agnostic to the source of uncertainty (aleatoric vs. epistemic) and to class identity, making it the most basic comparator against which our class-structured epistemic metrics are evaluated.

Mucsányi et al. (2024) – Benchmarking disentanglement. Mucsányi et al. [2024] conduct a large-scale benchmark of uncertainty quantification methods and find that the aleatoric and epistemic components produced by standard decomposition formulas are highly rank-correlated across distributional methods: $\rho(u_a, u_e) \geq 0.88$ on CIFAR-10 and $\rho(u_a, u_e) \geq 0.78$ on

ImageNet-1k. They interpret this as evidence that current methods fail to disentangle AU from EU, a conclusion that de Jong et al. [2026] subsequently show requires qualification.

de Jong et al. (2026) – Orthogonality as the correct criterion. de Jong et al. [2026] formalise what it means for AU and EU estimates to be *disentangled*. They define two requirements, *consistency* (each estimate correlates with its corresponding ground-truth uncertainty) and *orthogonality* (each estimate is insensitive to changes in the *other* ground-truth uncertainty), and prove that both are necessary and sufficient for disentanglement (their Theorems 3.1–3.3).

A central theoretical result (Theorem 3.2) is that on complex datasets where aleatoric noise and epistemic difficulty co-occur, a high correlation between the *estimators* u_a and u_e is a *necessary consequence of estimator validity*, not a sign of failure; Mucsányi et al. [2024]’s high- ρ finding is therefore consistent with well-calibrated models on correlated datasets. The correct diagnostic is orthogonality, formalised as their Uncertainty Disentanglement Error (UDE). Evaluating a range of methods across multiple datasets, de Jong et al. find that Deep Ensembles with Information-Theoretic (IT) disentanglement achieve the best UDE, but that no current method fully satisfies both consistency and orthogonality.

Critically for our work, de Jong et al. [2026] show that disentanglement behaviour is strongly modulated by whether the model is trained from scratch or fine-tuned from a pretrained backbone (their Section 5, Figure 7). For a Deep Ensemble ResNet-18 pretrained on ImageNet-1k and fine-tuned to CIFAR-10, the UDE is substantially higher than for the same architecture trained from scratch (0.545 vs. 0.332), primarily because $|\rho(u_e, U_a)| = 0.985$ in the pretrained case, aleatoric and epistemic uncertainty are almost fully conflated, compared to $|\rho(u_e, U_a)| = 0.312$ for the from-scratch model. This finding is directly relevant to our Section 5, where we observe the same qualitative pattern independently: the C_k Taylor approximation degrades considerably when a frozen pretrained backbone replaces end-to-end Bayesian training, and the AU/EU entanglement of MI and $\sum_k C_k$ increases markedly in the transfer-learning regime.

Depeweg et al. (2018) – AU/EU decomposition via total variance. Depeweg et al. [2018] formalise the decomposition of predictive uncertainty into aleatoric and epistemic components for latent-variable models. Applying the law of total variance to the predictive distribution $p(y | x)$ marginalised over the posterior $p(\omega | \mathcal{D})$ yields:

$$\underbrace{\text{Var}[y | x]}_{\text{total}} = \underbrace{\mathbb{E}_\omega[\text{Var}[y | x, \omega]]}_{\text{aleatoric}} + \underbrace{\text{Var}_\omega[\mathbb{E}[y | x, \omega]]}_{\text{epistemic}}. \quad (20)$$

This identity is the regression analogue of the information-theoretic decomposition $\text{MI} = H(\boldsymbol{\mu}) - \mathbb{E}[H(\boldsymbol{p})]$ used in classification; it also underlies the label-wise variance measures of Sale et al. [2024], which interpret $\text{Var}(\Theta_k)$ as the epistemic contribution from class k via the same total-variance decomposition applied marginally.

B PROOFS

B.1 PROOF OF THEOREM 2.2 (MI APPROXIMATION)

Proof. Expand $H(\boldsymbol{p}^{(s)})$ to second order around $\boldsymbol{\mu}$:

$$H(\boldsymbol{p}^{(s)}) \approx H(\boldsymbol{\mu}) + \nabla H(\boldsymbol{\mu})^\top (\boldsymbol{p}^{(s)} - \boldsymbol{\mu}) + \frac{1}{2} (\boldsymbol{p}^{(s)} - \boldsymbol{\mu})^\top \nabla^2 H(\boldsymbol{\mu}) (\boldsymbol{p}^{(s)} - \boldsymbol{\mu}). \quad (21)$$

Take expectations over the S passes. The linear term vanishes by definition of $\boldsymbol{\mu} = \mathbb{E}[\boldsymbol{p}^{(s)}]$. By Lemma 2.1 the Hessian is $\nabla^2 H(\boldsymbol{\mu}) = \text{diag}(-1/\mu_1, \dots, -1/\mu_K)$, so the quadratic term becomes

$$\frac{1}{2} \mathbb{E}[(\boldsymbol{p} - \boldsymbol{\mu})^\top \nabla^2 H(\boldsymbol{\mu}) (\boldsymbol{p} - \boldsymbol{\mu})] = \frac{1}{2} \text{tr}[\nabla^2 H(\boldsymbol{\mu}) \text{Cov}[\boldsymbol{p}]] = -\frac{1}{2} \sum_{k=1}^K \frac{\text{Var}[p_k]}{\mu_k}. \quad (22)$$

The second equality uses the fact that the Hessian is diagonal, so the trace selects only the diagonal elements of $\text{Cov}[\boldsymbol{p}]$: $\text{tr}[\text{diag}(-1/\mu_k) \text{Cov}[\boldsymbol{p}]] = -\sum_k \text{Var}[p_k]/\mu_k$. Substituting into (3) gives

$$\mathcal{I}(y; \boldsymbol{\omega} | x) = H(\boldsymbol{\mu}) - \mathbb{E}[H(\boldsymbol{p})] \approx \frac{1}{2} \sum_{k=1}^K \frac{\text{Var}[p_k](x)}{\mu_k(x)}, \quad (23)$$

with remainder $O(\mathbb{E}[\|\boldsymbol{p} - \boldsymbol{\mu}\|^3])$ from the discarded cubic terms. \square

Remark on the simplex constraint. The constraint $\sum_k p_k = 1$ forces $\sum_k (p_k - \mu_k) = 0$, so $\text{Cov}[\mathbf{p}]$ has zero row- and column-sums and rank at most $K - 1$. This does not invalidate the trace formula: the approximation operates on the full K -dimensional covariance, and the simplex constraint is already absorbed into the empirical estimates (1)–(2). Summing (6) over all K classes therefore remains valid.

B.2 PROOFS OF LEMMAS 2.4 AND 2.5

Proof of Lemma 2.4 (Variance Bound on the Simplex). Since $p_k^{(s)} \in [0, 1]$ implies $(p_k^{(s)})^2 \leq p_k^{(s)}$, we have

$$\text{Var}[p_k] = \mathbb{E}[p_k^2] - \mu_k^2 \leq \mathbb{E}[p_k] - \mu_k^2 = \mu_k - \mu_k^2 = \mu_k(1 - \mu_k). \quad (24)$$

Since $\mu_k(1 - \mu_k) \rightarrow 0$ as $\mu_k \rightarrow 0$ or $\mu_k \rightarrow 1$, we have $\text{Var}[p_k] \rightarrow 0$ at the simplex boundary regardless of the degree of disagreement among the S forward passes. \square

Proof of Lemma 2.5 (Boundary Behaviour of C_k). Dividing both sides of (9) by $2\mu_k > 0$:

$$C_k = \frac{1}{2} \frac{\text{Var}[p_k]}{\mu_k} \leq \frac{1}{2} \frac{\mu_k(1 - \mu_k)}{\mu_k} = \frac{1}{2}(1 - \mu_k). \quad (25)$$

As $\mu_k \rightarrow 0$, the upper bound $\frac{1}{2}(1 - \mu_k) \rightarrow \frac{1}{2}$, so C_k is not forced to zero near the simplex boundary. \square

Remark on attainability. The variance bound is tight: it is attained when $p_k^{(s)} \in \{0, 1\}$ for all s , i.e., each forward pass is maximally confident about class k but the passes disagree on the direction. In this case $\text{Var}[p_k] = \mu_k(1 - \mu_k)$ and $C_k = \frac{1}{2}(1 - \mu_k) \approx \frac{1}{2}$ for $\mu_k \ll 1$: exactly the non-vanishing signal that motivates the normalisation.

B.3 PROOF OF THEOREM 2.6

We follow the axiomatic framework of Wimmer et al. [2023], as extended by Sale et al. [2024]. Throughout, $Q \in \Delta_K^{(2)}$ is a second-order distribution over probability vectors $\mathbf{p} \in \Delta^{K-1}$, with mean $\boldsymbol{\mu} = \mathbb{E}_Q[\mathbf{p}]$. We write $\text{EU}(Q) = \sum_{k=1}^K C_k = \frac{1}{2} \sum_{k=1}^K \text{Var}[p_k]/\mu_k$.

Axioms evaluated.

- **A0** (Non-negativity): $\text{EU}(Q) \geq 0$.
- **A1** (Vanishing at certainty): $\text{EU}(Q) = 0$ iff $Q = \delta_{\boldsymbol{\theta}}$ for some $\boldsymbol{\theta} \in \Delta^{K-1}$.
- **A2** (Maximality at uniform): EU is maximised when $Q = Q_{\text{unif}}$, the uniform distribution on Δ^{K-1} .
- **A3** (Monotone under MPS, strict version): if Q' is a mean-preserving spread of Q then $\text{EU}(Q') > \text{EU}(Q)$.
- **A5** (Location-shift invariance): if Q' is a spread-preserving location shift of Q then $\text{EU}(Q') = \text{EU}(Q)$.

Definitions. Following Sale et al. [2024] (Definition 2.1), Q' is a *mean-preserving spread* (MPS) of Q if $\mathbf{p}' \stackrel{d}{=} \mathbf{p} + \mathbf{Z}$ where \mathbf{Z} satisfies $\mathbb{E}[\mathbf{Z} \mid \sigma(\mathbf{p})] = \mathbf{0}$ a.s. and $\max_k \text{Var}[Z_k] > 0$. Q' is a *spread-preserving location shift* of Q if $\mathbf{p}' \stackrel{d}{=} \mathbf{p} + \mathbf{z}$ for some constant $\mathbf{z} \neq \mathbf{0}$.

Proof. **A0.** $\text{Var}[p_k] = \mathbb{E}[p_k^2] - \mu_k^2 \geq 0$ by Jensen's inequality. When $\mu_k > 0$, $C_k = \frac{1}{2} \text{Var}[p_k]/\mu_k \geq 0$. When $\mu_k = 0$: $p_k \geq 0$ and $\mathbb{E}[p_k] = 0$ imply $p_k = 0$ Q -a.s., so $\text{Var}[p_k] = 0$ and $C_k := 0$ by convention. Hence $\text{EU}(Q) = \sum_k C_k \geq 0$.

A1. (\Rightarrow) If $Q = \delta_{\boldsymbol{\theta}}$, then $\text{Var}[p_k] = 0$ for every k , so $\text{EU}(Q) = 0$. (\Leftarrow) Suppose $\text{EU}(Q) = 0$. Since each $C_k \geq 0$ and $\sum_k C_k = 0$, every $C_k = 0$. For $\mu_k > 0$ this forces $\text{Var}[p_k] = 0$, hence $p_k = \mu_k$ Q -a.s. For $\mu_k = 0$, $p_k = 0 = \mu_k$ Q -a.s. by non-negativity of p_k . Hence $\mathbf{p} = \boldsymbol{\mu}$ Q -a.s., i.e. $Q = \delta_{\boldsymbol{\mu}}$.

A3 (strict). Let $\mathbf{p}' \stackrel{d}{=} \mathbf{p} + \mathbf{Z}$ with $\mathbb{E}[\mathbf{Z} \mid \sigma(\mathbf{p})] = \mathbf{0}$ a.s. and $\max_k \text{Var}[Z_k] > 0$.

Mean preservation. $\mu'_k = \mathbb{E}[p_k + Z_k] = \mu_k + \mathbb{E}[\mathbb{E}[Z_k \mid \sigma(\mathbf{p})]] = \mu_k$.

Variance expansion.

$$\text{Var}[p'_k] = \text{Var}[p_k + Z_k] = \text{Var}[p_k] + \text{Var}[Z_k] + 2 \text{Cov}[p_k, Z_k]. \quad (26)$$

The cross-term vanishes by the tower property and $\sigma(\mathbf{p})$ -measurability of p_k :

$$\text{Cov}[p_k, Z_k] = \mathbb{E}[p_k Z_k] - \mathbb{E}[p_k] \mathbb{E}[Z_k] = \mathbb{E}\left[\mathbb{E}[p_k Z_k \mid \sigma(\mathbf{p})]\right] - \mathbb{E}[p_k] \cdot \mathbb{E}\left[\mathbb{E}[Z_k \mid \sigma(\mathbf{p})]\right] = \mathbb{E}\left[p_k \underbrace{\mathbb{E}[Z_k \mid \sigma(\mathbf{p})]}_{=0}\right] - \mathbb{E}[p_k] \cdot 0 = 0. \quad (27)$$

Hence $\text{Var}[p'_k] = \text{Var}[p_k] + \text{Var}[Z_k]$, and since $\mu'_k = \mu_k$, we have $C_k(Q') \geq C_k(Q)$ for all k .

Strict increase. By the MPS condition, $\text{Var}[Z_j] > 0$ for some j . We show $\mu_j > 0$. If $\mu_j = 0$ then $p_j = 0$ Q -a.s., so $p'_j = Z_j$. Since $\mathbf{p}' \in \Delta^{K-1}$, we have $p'_j \geq 0$, hence $Z_j \geq 0$ Q -a.s. Combined with $\mathbb{E}[Z_j] = \mathbb{E}[\mathbb{E}[Z_j \mid \sigma(\mathbf{p})]] = 0$, this forces $Z_j = 0$ Q -a.s., contradicting $\text{Var}[Z_j] > 0$. Hence $\mu_j > 0$, giving $C_j(Q') = \frac{1}{2}(\text{Var}[p_j] + \text{Var}[Z_j])/\mu_j > C_j(Q)$, and therefore $\text{EU}(Q') > \text{EU}(Q)$.

A2 violated. Lemma 2.4 gives $\text{Var}[p_k] \leq \mu_k(1 - \mu_k)$, so

$$\text{EU}(Q) = \frac{1}{2} \sum_{k=1}^K \frac{\text{Var}[p_k]}{\mu_k} \leq \frac{1}{2} \sum_{k=1}^K (1 - \mu_k) = \frac{K-1}{2}, \quad (28)$$

using $\sum_k \mu_k = 1$. The bound is attained by the uniform vertex mixture $Q_{\text{vert}} = \frac{1}{K} \sum_{y=1}^K \delta_{\mathbf{e}_y}$, for which $\mu_k = 1/K$, $\text{Var}[p_k] = \mathbb{E}[p_k^2] - \mu_k^2 = 1/K - 1/K^2 = (K-1)/K^2$, and $\text{EU}(Q_{\text{vert}}) = (K-1)/2$. By contrast, the uniform distribution on Δ^{K-1} equals Dirichlet($\mathbf{1}_K$), whose marginals satisfy $\text{Var}[p_k] = (K-1)/[K^2(K+1)]$ (standard Dirichlet second moment), giving

$$\text{EU}(Q_{\text{unif}}) = K \cdot \frac{1}{2} \cdot \frac{(K-1)/[K^2(K+1)]}{1/K} = \frac{K-1}{2(K+1)} < \frac{K-1}{2} = \text{EU}(Q_{\text{vert}}) \quad \forall K \geq 2. \quad (29)$$

Hence Q_{unif} is not the maximiser and A2 is violated.

A5 violated. Under $\mathbf{p}' = \mathbf{p} + \mathbf{z}$ (constant \mathbf{z}): $\text{Var}[p'_k] = \text{Var}[p_k]$ by translation-invariance of variance, but $\mu'_k = \mu_k + z_k$, so $C_k(Q') = \frac{1}{2} \text{Var}[p_k]/(\mu_k + z_k) \neq C_k(Q)$ whenever $z_k \neq 0$ and $\text{Var}[p_k] > 0$. Concretely, let $K = 2$ and $Q = \frac{1}{2} \delta_{(0.2, 0.8)} + \frac{1}{2} \delta_{(0.4, 0.6)}$, so $\boldsymbol{\mu} = (0.3, 0.7)$, $\text{Var}[p_k] = 0.01$ for both k , and $\text{EU}(Q) \approx 0.0238$. Under $\mathbf{z} = (0.15, -0.15)$: $\boldsymbol{\mu}' = (0.45, 0.55)$, variances unchanged, giving $\text{EU}(Q') \approx 0.0202 \neq \text{EU}(Q)$. \square

Remark B.1 (Wimmer et al. [2023] Proposition 4). Exact MI violates the strict version of A3 already for $K = 2$. The improvement of $\sum_k C_k$ is a direct consequence of its linearity in $\{\text{Var}[p_k]\}$: any non-trivial spread in any class propagates immediately into a strict increase of the aggregate.

Table 5: Axiomatic profile of epistemic uncertainty measures. \checkmark = satisfied, \times = violated. Exact MI results from Wimmer et al. [2023]; Sale et al. results from Sale et al. [2024].

Axiom	$\sum_k C_k$ (ours)	Exact MI	$\text{Var}(\Theta_k)$
A0: Non-negativity	\checkmark	\checkmark	\checkmark
A1: Vanishing EU	\checkmark	\checkmark	\checkmark
A2: Maximality at uniform	\times	\times	\times
A3: Monotonicity (MPS)	\checkmark	\times	\checkmark
A5: Location-shift invariance	\times	\times	\checkmark

C COMPLETE METRIC REFERENCE

This appendix collects, in self-contained form, the definitions and interpretations of every uncertainty metric evaluated in the selective prediction experiments. Throughout, we adopt the notation of Section 2: S stochastic forward passes produce probability vectors $\mathbf{p}^{(s)}(x) \in \Delta^{K-1}$, $s = 1, \dots, S$, from which all subsequent quantities are estimated.

C.1 MONTE CARLO PREDICTION STATISTICS

The following sample statistics, computed from the S stochastic forward passes, serve as building blocks for all metrics defined below.

Mean prediction. The predictive mean

$$\mu_k = \frac{1}{S} \sum_{s=1}^S p_k^{(s)}, \quad k = 0, \dots, K-1, \quad (30)$$

represents the model’s consensus probability for class k . The predicted label is $\hat{y} = \arg \max_k \mu_k$.

Per-class variance and covariance. The sample variance and covariance, with Bessel correction, are

$$\sigma_k^2 = \frac{1}{S-1} \sum_{s=1}^S (p_k^{(s)} - \mu_k)^2, \quad (31)$$

$$\Sigma_{ij} = \frac{1}{S-1} \sum_{s=1}^S (p_i^{(s)} - \mu_i)(p_j^{(s)} - \mu_j), \quad (32)$$

with Pearson correlation $\rho_{ij} = \Sigma_{ij}/(\sigma_i \sigma_j)$. A strongly negative ρ_{ij} indicates that probability mass flows systematically from class j to class i across forward passes—i.e. the model actively confuses the two classes.

Third central moment.

$$m_{3,k} = \frac{1}{S} \sum_{s=1}^S (p_k^{(s)} - \mu_k)^3. \quad (33)$$

This quantity enters only through the skewness diagnostic ρ_k defined in Section C.7.

C.2 SCALAR UNCERTAINTY BASELINES

The following standard metrics assign a single uncertainty score to each input and do not distinguish between classes.

Predictive entropy. The Shannon entropy of the mean prediction,

$$H[\bar{p}] = - \sum_{k=0}^{K-1} \mu_k \log \mu_k, \quad (34)$$

lies in $[0, \log K]$ and captures *total* predictive uncertainty—both epistemic and aleatoric. It cannot distinguish a model that lacks training data from one facing a genuinely ambiguous input; nor does it differentiate clinically benign confusions (e.g. Grade 0 vs. Grade 1) from dangerous ones (Grade 0 vs. Grade 3).

Mutual information.

$$\text{MI} = H[\bar{p}] - \frac{1}{S} \sum_{s=1}^S H[\mathbf{p}^{(s)}], \quad (35)$$

where $H[\mathbf{p}^{(s)}] = - \sum_k p_k^{(s)} \log p_k^{(s)}$. MI isolates epistemic uncertainty by subtracting the average per-pass entropy (the aleatoric component): if all S passes produce identical softmax vectors, MI vanishes regardless of how uncertain those vectors are. While MI is the standard scalar epistemic measure, it remains a single number that cannot reveal *which* classes drive the model’s disagreement. Two inputs with identical MI may involve entirely different confusion patterns, as demonstrated by the error signatures in Section D.9.

Maximum softmax uncertainty.

$$\text{MaxProb} = 1 - \max_k \mu_k. \quad (36)$$

This is the simplest deferral baseline: it uses only the mean prediction and does not exploit MC disagreement. MaxProb is insensitive to the *distribution* of probability across non-top classes; two inputs $\mu = (0.6, 0.4, 0, 0)$ and $\mu = (0.6, 0, 0.4, 0)$ receive identical scores despite the latter involving a dangerous safe–critical confusion.

C.3 PER-CLASS VARIANCE BASELINES

These metrics use the raw per-class variance σ_k^2 as a proxy for epistemic disagreement, without the $1/\mu_k$ normalisation that defines C_k .

Critical variance.

$$\text{Var_crit} = \max_{k \in \mathcal{C}} \sigma_k^2, \quad (37)$$

where $\mathcal{C} = \{2, 3\}$ denotes the set of critical (treatment-requiring) classes. This provides a targeted measure of MC disagreement restricted to critical classes, but inherits the base-rate confound identified in Lemma 2.4: a class with $\mu_k = 0.5$ naturally exhibits higher variance than one with $\mu_k = 0.01$, even at equal levels of epistemic disagreement in logit space.

Global and critical variance baselines. Sale et al. [2024] explicitly define the global variance-based epistemic uncertainty measure (their equation 22):

$$\text{Sale_EU_global} = \sum_{k=0}^{K-1} \sigma_k^2, \quad (38)$$

which aggregates label-wise variance over all classes and constitutes a scalar epistemic measure directly comparable to MI and $\sum_k C_k$. We additionally construct a critical-class restriction not defined by Sale et al. [2024]:

$$\text{Sale_EU_crit} = \sum_{k \in \mathcal{C}} \sigma_k^2, \quad (39)$$

which provides a targeted analogue of $C_{\text{crit_sum}}$ without curvature normalisation. Both variants suffer from the same boundary suppression as Var_crit : for critical classes with mean prediction $\mu_k \approx 0.06$ in our data, variance is bounded by $\mu_k(1 - \mu_k) \approx 0.056$ regardless of the degree of model disagreement (cf. Section 2.3).

C.4 ONE-VS-ALL MI BASELINE

An alternative per-class decomposition computes binary mutual information for each class independently. For class k , define the binary variable $q_k^{(s)} = (p_k^{(s)}, 1 - p_k^{(s)})$ and the corresponding binary MI

$$\text{MI}_k^{\text{bin}} = H[\bar{q}_k] - \frac{1}{S} \sum_{s=1}^S H[q_k^{(s)}]. \quad (40)$$

The deferral score sums over critical classes: $\text{OvA_MI} = \sum_{k \in \mathcal{C}} \text{MI}_k^{\text{bin}}$. This measure is exact (not Taylor-approximated) but discards the multi-class structure: it does not reveal which non- k classes compete with class k , and the per-class binary MI terms are not additive components of the full multiclass MI.

C.5 PROPOSED METRICS: PER-CLASS EPISTEMIC DECOMPOSITION

The metrics in this subsection are derived from the second-order Taylor expansion of mutual information developed in Section 2.

Per-class epistemic contribution. The central quantity is the per-class component

$$C_k = \frac{1}{2} \frac{\sigma_k^2}{\mu_k} \quad (41)$$

which satisfies $\sum_{k=0}^{K-1} C_k \approx \text{MI}$ by Theorem 2.2. The $1/\mu_k$ weighting originates from the curvature of the entropy surface ($\partial^2 H / \partial p_k^2 = -1/\mu_k$): a class with $\mu_k = 0.01$ has curvature 100, so even modest probability variance there carries substantial information-theoretic weight, whereas a class with $\mu_k = 0.5$ requires proportionally larger variance to indicate genuine epistemic uncertainty. The ratio σ_k^2/μ_k coincides with the classical index of dispersion [Cox and Lewis, 1966, Fano, 1947]; the $\frac{1}{2}$ prefactor arises from the Hessian structure, ensuring that the components sum to MI rather than twice MI.

The approximation is reliable when the MC distribution for each class is approximately symmetric. Reliability is diagnosed by the skewness indicator ρ_k (Section C.7): when $\rho_k > 0.3$ for a critical class, C_k should be interpreted with caution and CBEC (Section C.6) is preferred.

Critical-class aggregations. Two natural aggregations restrict attention to the critical class set \mathcal{C} :

$$C_{\text{crit_max}} = \max_{k \in \mathcal{C}} C_k, \quad (42)$$

$$C_{\text{crit_sum}} = \sum_{k \in \mathcal{C}} C_k. \quad (43)$$

$C_{\text{crit_max}}$ is sensitive to single-class spikes: it fires when *any* critical class carries elevated epistemic uncertainty, and is the recommended aggregation when $\rho_k < 0.3$ for all critical classes. $C_{\text{crit_sum}}$ is a smoother alternative that captures cumulative uncertainty when confusion is distributed across multiple critical classes.

C.6 BOUNDARY-AWARE METRICS

The metrics above score each class (or class subset) in isolation. In applications with a clinically meaningful partition into safe classes $\mathcal{S} = \{0, 1\}$ and critical classes $\mathcal{C} = \{2, 3\}$, the most dangerous errors are those that cross this boundary. The following metric targets such cross-boundary confusion directly.

Cross-boundary epistemic confusion (CBEC).

$$\text{CBEC}(x) = \sum_{i \in \mathcal{S}} \sum_{j \in \mathcal{C}} \sqrt{C_i \cdot C_j} \cdot \max(0, -\rho_{ij}). \quad (44)$$

CBEC is non-zero only when three conditions hold simultaneously: a safe class carries elevated C_i , a critical class carries elevated C_j , and their MC predictions are negatively correlated ($\rho_{ij} < 0$), indicating that probability mass flows systematically from one to the other across stochastic passes. The geometric mean $\sqrt{C_i C_j}$ requires *both* classes to be uncertain, and the correlation gate $\max(0, -\rho_{ij})$ filters coincidental co-elevation.

CBEC is partially robust to degradation of the Taylor approximation for two reasons. First, the correlation ρ_{ij} is computed directly from MC samples and does not depend on the second-order expansion. Second, the geometric mean compresses outlier inflation: if skewness inflates C_j by a factor of α , the geometric mean is inflated by only $\sqrt{\alpha}$. These properties explain CBEC’s empirical robustness under MC dropout, where C_k estimates for rare critical classes degrade (Section D.11).

C.7 DIAGNOSTIC METRICS

The following quantities assess the reliability and structure of the C_k estimates. They are not used as deferral scores.

Skewness diagnostic. For each class k with $\sigma_k^2 > 0$, the ratio

$$\rho_k = \frac{|m_{3,k}|}{3 \mu_k \cdot \sigma_k^2} \quad (45)$$

equals the magnitude of the third-order Taylor correction relative to the second-order term C_k (see Section 2.5). When $\rho_k \ll 1$, the cubic remainder is negligible and C_k is reliable; when $\rho_k > 0.3$, the second-order approximation is degrading and C_k should be supplemented or replaced by CBEC. In practice, majority classes (high μ_k , far from the simplex boundary) produce approximately symmetric MC distributions and low ρ_k ; rare classes ($\mu_k \approx 0$) produce right-skewed distributions bounded by zero and correspondingly higher ρ_k .

Epistemic profiles. For each true class i , the normalised conditional expectation

$$\text{Profile}_k(i) = \mathbb{E}\left[\frac{C_k}{\sum_j C_j} \mid y = i\right], \quad k = 0, \dots, K-1, \quad (46)$$

reveals the average distribution of epistemic uncertainty across classes for inputs of true class i . For example, a profile (0.14, 0.27, 0.55, 0.05) for Grade 0 images indicates that the model’s uncertainty about healthy images concentrates predominantly on Grade 2 (moderate DR), signalling systematic Grade 0–Grade 2 confusion.

Error epistemic signatures. Conditioning on both true and predicted labels yields the error-type signature

$$\text{Sig}_k(i \rightarrow j) = \mathbb{E}[C_k \mid y = i, \hat{y} = j], \quad k = 0, \dots, K-1. \quad (47)$$

Different error types produce distinct C_k fingerprints even when their scalar MI is similar, enabling targeted diagnostic interpretation (see Section D.9).

Epistemic confusion matrix.

$$E_{ij} = \mathbb{E}[\sqrt{C_i \cdot C_j} \cdot \max(0, -\rho_{ij})]. \quad (48)$$

Entry E_{ij} quantifies the average directed epistemic confusion between classes i and j , aggregated over the test set. The matrix is symmetric with zero diagonal (since $\rho_{kk} = 1$ implies $\max(0, -\rho_{kk}) = 0$). High values in the $\mathcal{S} \times \mathcal{C}$ block indicate that the model’s epistemic uncertainty concentrates at the clinically dangerous boundary, validating both the safe–critical partition and the CBEC aggregation.

C.8 EVALUATION METRICS FOR SELECTIVE PREDICTION

The following metrics evaluate the quality of a deferral policy that, at coverage level c , retains a fraction c of test inputs for autonomous prediction and defers the remainder to human review. Let $\text{kept}(c)$ denote the set of retained samples.

Critical false-negative rate.

$$\text{Critical FNR}(c) = \frac{\sum_{n \in \text{kept}(c)} \mathbb{1}[y_n \in \mathcal{C}] \cdot \mathbb{1}[\hat{y}_n \notin \mathcal{C}]}{\sum_{n \in \text{kept}(c)} \mathbb{1}[y_n \in \mathcal{C}]}. \quad (49)$$

This is the primary clinical safety metric: among the critical-class samples that the system decides autonomously (does not defer), it measures the fraction misclassified as safe. Crucially, within-critical errors (e.g. Grade 3 predicted as Grade 2) are *not* counted, since the patient still receives treatment; only boundary crossings into \mathcal{S} are penalised.

Critical error rate.

$$\text{Critical Err}(c) = \frac{\sum_{n \in \text{kept}(c)} \mathbb{1}[y_n \in \mathcal{C}] \cdot \mathbb{1}[\hat{y}_n \neq y_n]}{\sum_{n \in \text{kept}(c)} \mathbb{1}[y_n \in \mathcal{C}]}. \quad (50)$$

A broader metric that includes within-critical misclassifications. We report it alongside Critical FNR for completeness but consider Critical FNR the primary safety metric.

Area under the selective risk curve (AUSC).

$$\text{AUSC} = \int_0^1 R(c) dc, \quad (51)$$

where $R(c)$ is the risk (Critical FNR or error rate) at coverage c [El-Yaniv and Wiener, 2010]. AUSC provides a single-number summary that integrates risk over all possible operating points, so a policy with low AUSC is consistently safe regardless of the chosen coverage threshold. We approximate the integral via the trapezoidal rule at $n = 200$ equally spaced coverage levels; 95% confidence intervals are obtained from 200 bootstrap resamples of the test set.

Note that AUSC and Critical FNR at a fixed operating point can disagree: a policy that dominates at low coverages (50–70%) but is inferior at 80% will produce favourable AUSC yet a suboptimal fixed-point FNR. This phenomenon appears in the MC dropout experiment (Section D.11).

Accuracy and macro F1. Standard classification metrics computed on the retained set:

$$\text{Accuracy}(c) = \frac{\sum_{n \in \text{kept}(c)} \mathbb{1}[\hat{y}_n = y_n]}{|\text{kept}(c)|}, \quad \text{Macro F1}(c) = \frac{1}{K} \sum_{k=0}^{K-1} F_{1,k}. \quad (52)$$

In our setting, accuracy is dominated by the majority class (Grade 0 constitutes approximately 70% of the test set) and can be misleading: a policy that defers all minority-class samples achieves high accuracy but poor safety. Macro F1 partially corrects the class-prevalence bias by weighting classes equally, but remains an aggregate metric that does not specifically target clinical safety. We report both alongside the primary Critical FNR.

D DIABETIC RETINOPATHY EXPERIMENT: SUPPLEMENTARY DETAILS

D.1 DATASET AND PREPROCESSING

We pool three public DR grading datasets: EyePACS (35,108 images), APTOS 2019 (3,662), and Messidor-2 (1,200), totalling 39,970 fundus images. The original five-level International Clinical DR Scale is consolidated into four grades: Grade 0 (no DR, 70.4%), Grade 1 (mild NPDR, 7.4%), Grade 2 (moderate NPDR, 16.3%), and Grade 3 (severe NPDR + PDR, 5.8%). We merge the two highest grades because both require urgent referral, and the small severe NPDR subgroup is insufficient for reliable posterior estimation.

Images are resized to 256×256 pixels. Data are split patient-stratified into train/val/test = 28,018/4,004/7,948, with a patient-leakage check confirming no patient appears in multiple splits. The test set preserves the class distribution: Grade 0 = 5,584 (70.3%), Grade 1 = 587 (7.4%), Grade 2 = 1,322 (16.6%), Grade 3 = 455 (5.7%).

D.2 MODEL ARCHITECTURE AND TRAINING

Bayesian EfficientNet-B4. We construct a fully Bayesian variant of EfficientNet-B4 (width multiplier 1.4, depth multiplier 1.8) using the low-rank variational framework of Toure and Stephens [2026], which parameterises each weight matrix as $W = AB^\top$ with learned posteriors on the factors $A \in \mathbb{R}^{m \times r}$, $B \in \mathbb{R}^{n \times r}$, reducing the parameter count from $O(mn)$ to $O(r(m+n))$. The architecture comprises a stem convolution (3 \rightarrow 48 filters), 32 MBConv blocks across 7 stages, a top expansion (448 \rightarrow 1792), and a classification head (Conv 1792 \rightarrow 256, GAP, Dense 256 \rightarrow 128, Dropout, Dense 128 \rightarrow 4).

Pointwise (1×1) and expansion convolutions use low-rank factorisation $W = AB^\top$ with depth-aware rank selection: compression increases from $1.5 \times$ at early layers to $25 \times$ at deep layers, with rank $r = \lfloor d_{\text{in}} d_{\text{out}} / (\text{compression} \cdot (d_{\text{in}} + d_{\text{out}})) \rfloor$. Depthwise convolutions and squeeze-excitation 1×1 convolutions use direct (full-rank) variational parameterisation. Dense layers in the classification head use the same low-rank factorisation.

All variational layers use the local reparameterisation trick with $W = \mu + \text{softplus}(\rho) \odot \epsilon$, $\epsilon \sim \mathcal{N}(0, I)$. The prior is a scale-mixture Gaussian $\pi \mathcal{N}(0, \sigma_1^2) + (1 - \pi) \mathcal{N}(0, \sigma_2^2)$ with $\pi = 0.5$, $\sigma_1 = 1.0$, $\sigma_2 = e^{-6}$. Posterior initialisation uses He-scaled uniform means with ρ initialised so that $\text{softplus}(\rho) \approx 0.09 \sqrt{2/d_{\text{in}}}$. Training uses KL annealing with the scale frozen at zero for the first epochs, then linearly warmed up. BatchNormalization layers remain deterministic.

Full-rank layers. Depthwise convolutions lack the $m \times n$ matrix structure required for low-rank factorisation: each channel has an independent $k \times k$ kernel ($k \in \{3, 5\}$), so there is no shared row-column space on which to impose $W = AB^\top$. SE layers are already bottlenecked by the squeeze ratio ($r_{\text{SE}} = 0.25$), yielding weight matrices such as 112×28 that are smaller than the rank our depth-aware rule would select; further factorisation would over-compress the channel-attention mechanism. Both cases therefore use direct variational parameterisation with element-wise (μ, ρ) pairs.

MC Dropout baseline. We also train a standard (deterministic) EfficientNet-B4 with dropout ($p = 0.3$) before the final dense layer. At test time, dropout is kept active for $S = 30$ forward passes, producing MC dropout posterior samples.

Inference. For both models, uncertainty is computed from $S = 30$ stochastic forward passes, producing $\mathbf{p}^{(s)} \in \Delta^3$ for each test image. All metrics in Appendix C are computed from these S samples.

D.3 BASELINE CLASSIFICATION PERFORMANCE

Table 6 reports the Bayesian model’s per-class precision, recall, and F1 on the test set. The model achieves overall accuracy 0.794 and quadratic weighted kappa 0.646. Grade 1 (mild NPDR) is effectively undetectable (F1 = 0.00), consistent with its visual subtlety and small sample size; this does not affect our analysis since Grade 1 belongs to the safe class partition.

The confusion matrix reveals the dominant error modes: Grade 0 absorbs most misclassifications from all other grades (497 from Grade 1, 548 from Grade 2, 107 from Grade 3), reflecting the class imbalance and the model’s conservatism toward the majority class. Within the critical partition, 220 Grade 3 samples are predicted as Grade 2 (severity underestimate) and 39 Grade 2 samples as Grade 3.

Table 6: Classification report for Bayesian EfficientNet-B4 on DR test set ($n = 7,948$).

Class	Precision	Recall	F1	Support
Grade 0 (No DR)	0.83	0.98	0.89	5,584
Grade 1 (Mild)	0.00	0.00	0.00	587
Grade 2 (Moderate)	0.62	0.56	0.59	1,322
Grade 3 (Severe+PDR)	0.75	0.28	0.41	455
Macro avg	0.55	0.45	0.47	7,948
Weighted avg	0.73	0.79	0.75	7,948

D.4 SKEWNESS DIAGNOSTIC ANALYSIS

The skewness diagnostic ρ_k (Definition 2.10) assesses whether C_k is reliable for each class and sample. Table 7 reports per-class ρ_k statistics on the full test set.

Table 7: Skewness diagnostic ρ_k by grade (Bayesian model, $n = 7,948$). “Reliable” = fraction of samples with $\rho_k < 0.3$.

Grade	Median ρ_k	Mean ρ_k	p_{90}	Reliable
0 (No DR)	0.012	0.086	0.116	94.6%
1 (Mild)	0.037	0.082	0.135	97.0%
2 (Moderate)	0.124	0.198	0.423	81.6%
3 (Severe+PDR)	0.218	0.328	0.706	63.4%

Two patterns emerge. First, the safe classes (Grades 0–1) have consistently low ρ_k (median < 0.04 , $> 94\%$ reliable), because their high mean probabilities ($\mu_0 \approx 0.7$) place them far from the simplex boundary where skewness is amplified. Second, the critical classes show progressively higher skewness: Grade 2 (median $\rho_2 = 0.12$, 82% reliable) and Grade 3 (median $\rho_3 = 0.22$, 63% reliable), consistent with their low base rates pushing μ_k toward the boundary. Across the full test set, 57% of samples have *all* four $\rho_k < 0.3$. See Figure 3 for the full distribution.

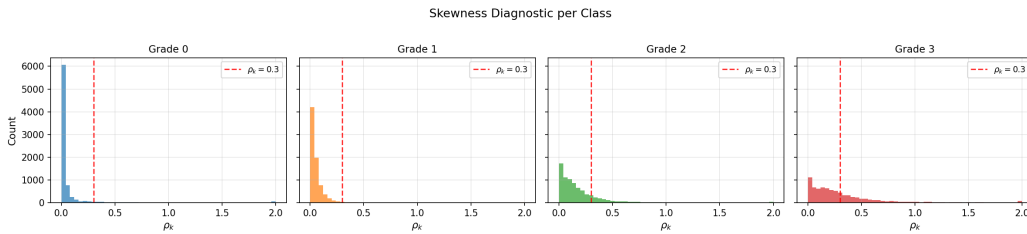


Figure 3: Distribution of skewness diagnostic ρ_k by class. Safe classes (Grades 0–1) cluster near zero; critical classes (Grades 2–3) exhibit heavier tails, reflecting boundary suppression effects on rare-class posterior samples.

These statistics explain the BNN ranking in Table 2: with the majority of critical-class C_k estimates reliable, $C_{\text{crit_max}}$ can exploit the per-class signal effectively. The MC dropout model (Appendix D.11) produces coarser posterior samples (fewer effective degrees of freedom), inflating ρ_k and degrading C_k for critical classes, which explains why CBEC, whose correlation gate is Taylor-free and whose restricted domain $\mathcal{S} \times \mathcal{C}$ filters irrelevant co-elevation, outperforms $C_{\text{crit_max}}$ in that regime.

D.5 THEORY VALIDATION: MI VS. $\sum_k C_k$

Figure 4 plots $\sum_k C_k$ against exact MI for all 7,948 test samples, complementing the summary statistics reported in Section 3.3. The slight systematic overestimation visible at high MI values is consistent with the third-order correction in Lemma 2.9: right-skewed distributions near the simplex boundary produce $m_{3,k} > 0$, and the omitted correction $-\frac{1}{6} \sum_k m_{3,k} / \mu_k^2$ causes $\sum_k C_k$ to slightly exceed MI. The right panel confirms this: residuals ($\sum_k C_k - \text{MI}$) are predomi-

nantly positive for high-skewness samples (pink/red points), validating that the skewness diagnostic ρ_k correctly identifies inputs where the approximation degrades.

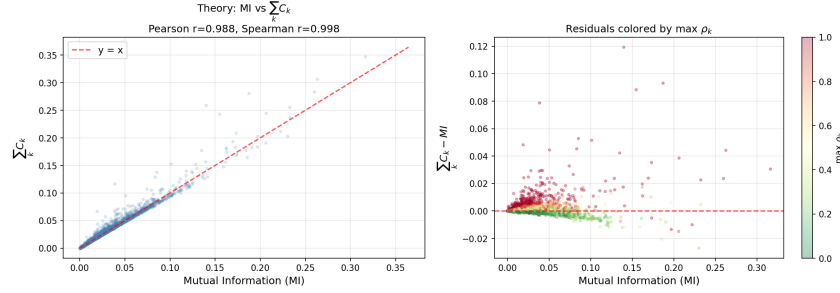


Figure 4: $\sum_k C_k$ vs. exact MI for all 7,948 test samples (Pearson $r = 0.988$, Spearman $r = 0.998$). **Left:** Scatter plot; the near-perfect rank correlation confirms that the second-order approximation preserves the ordering of epistemic uncertainty. **Right:** Residuals coloured by maximum per-class ρ_k ; positive residuals concentrate among high-skewness samples, as predicted by Lemma 2.9.

D.6 EXTENDED SELECTIVE PREDICTION ANALYSIS

Figure 5 shows the full selective risk curves for all 10 deferral policies across continuous coverage levels. The left panel (Critical FNR) confirms that C_{crit_max} achieves the lowest AUSC (0.285), with C_{crit_sum} second (0.329) and CBEC third (0.415). The gap widens at lower coverages where clinical operating points typically lie, and the unnormalised variance baselines (Sale_EU_crit: 0.650, Var_crit: 0.606) perform substantially worse than even scalar MI (0.436), confirming that boundary suppression severely degrades raw variance for rare critical classes.

The right panel addresses a natural concern: does targeting critical-class uncertainty sacrifice overall accuracy? The answer is no. C_{crit_max} achieves competitive error-rate AUSC (0.143), comparable to entropy (0.127) and MaxProb (0.126), which optimise for overall accuracy rather than safety. This demonstrates that the C_k decomposition identifies samples where critical-class confusion drives errors, rather than deferring difficult samples indiscriminately.

A further distinction emerges at the clinically relevant 80% coverage point: C_{crit_max} retains 1,293 critical samples (27.2% deferred) while achieving FNR 0.302, whereas MI retains only 1,183 (33.4% deferred) with FNR 0.339. C_{crit_max} is simultaneously *less aggressive* at deferring critical cases and *more accurate* on those it keeps, the hallmark of a well-targeted deferral policy. Entropy, by contrast, defers 42.1% of critical samples at 80% coverage because it prioritises total uncertainty rather than critical-class epistemic uncertainty.

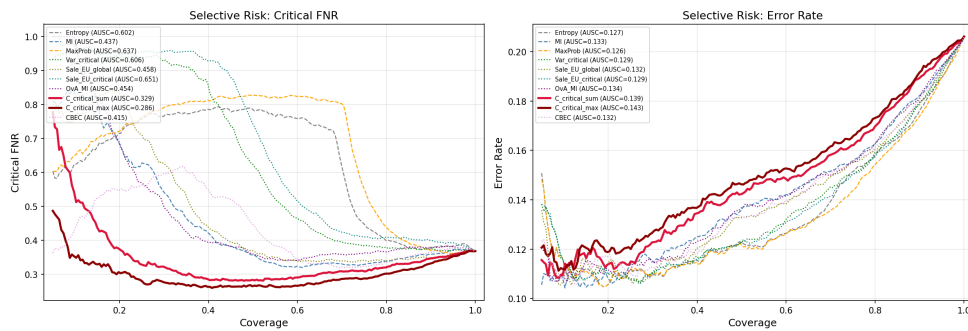


Figure 5: Selective risk curves for all 10 deferral policies. **Left:** Critical FNR across coverage levels; C_{crit_max} achieves the lowest AUSC (0.285), dominating all baselines across the full coverage range. **Right:** Error rate; C_{crit_max} remains competitive (AUSC = 0.143), confirming that per-class targeting does not sacrifice overall accuracy.

D.7 FULL BOOTSTRAP RESULTS: BAYESIAN MODEL

Table 8 extends Table 2 with all evaluated policies and additional metrics at 80% coverage. The ranking stability column reports the fraction of 200 bootstrap resamples in which each policy achieves the lowest AUSC.¹

Table 8: Full bootstrap results for Bayesian EfficientNet-B4 ($S=30$, 200 resamples). Policies ranked by AUSC (Critical FNR).

Family	Policy	AUSC↓	Critical FNR @80%↓	Acc @80%↑	Win%
Per-class C_k	C_{crit_max}	0.285 ± 0.016	0.302 ± 0.013	0.827 ± 0.005	50.5
Per-class C_k	C_{crit_sum}	0.327 ± 0.017	0.321 ± 0.014	0.831 ± 0.005	0.0
Boundary	CBEC	0.416 ± 0.020	0.335 ± 0.014	0.840 ± 0.005	0.0
Scalar	MI	0.436 ± 0.019	0.339 ± 0.014	0.838 ± 0.005	0.0
Per-class MI	OvA_MI	0.452 ± 0.017	0.367 ± 0.015	0.838 ± 0.005	0.0
Per-class var.	Sale_EU_global	0.457 ± 0.018	0.341 ± 0.015	0.840 ± 0.005	0.0
Scalar	Entropy	0.604 ± 0.022	0.401 ± 0.016	0.842 ± 0.005	0.0
Per-class var.	Var_crit	0.606 ± 0.014	0.379 ± 0.016	0.842 ± 0.005	0.0
Scalar	MaxProb	0.639 ± 0.022	0.439 ± 0.017	0.846 ± 0.005	0.0
Per-class var.	Sale_EU_crit	0.650 ± 0.013	0.409 ± 0.016	0.843 ± 0.005	0.0

Pairwise statistical significance. Table 9 reports bootstrap pairwise comparisons for the proposed methods against key baselines. $P(\text{row} < \text{col})$ denotes the fraction of bootstrap resamples in which the row policy achieves lower AUSC than the column policy; values above 0.975 indicate significance at the 5% level (two-tailed).

Table 9: Bootstrap pairwise comparisons (BNN). Entry = $P(\text{row AUSC} < \text{col AUSC})$.

	MI	Var_crit	Sale_EU_crit
C_{crit_max}	1.000***	1.000***	1.000***
C_{crit_sum}	1.000***	1.000***	1.000***
CBEC	0.950	1.000***	1.000***

D.8 EPISTEMIC PROFILES

Table 10 reports the normalised epistemic mass $\mathbb{E}[C_k / \sum_j C_j \mid y = i]$, showing which classes absorb epistemic uncertainty for each true label. Figure 6 visualises both the raw and normalised profiles as heatmaps.

Table 10: Normalised epistemic profiles: $\mathbb{E}[C_k / \sum_j C_j \mid y=i]$ (Bayesian model). Each row sums to 100%. Bold = dominant component.

True class	C_0	C_1	C_2	C_3
Grade 0	12.3%	32.7%	50.9%	4.0%
Grade 1	22.0%	24.8%	47.1%	6.1%
Grade 2	34.6%	18.2%	31.0%	16.2%
Grade 3	21.4%	15.7%	40.2%	22.7%

Grade 2 is the dominant source of epistemic uncertainty across all true classes, consistent with it being the most confusable category (moderate DR is clinically subtle). For true Grade 0 and Grade 1, over 50% and 47% of the epistemic mass concentrates on C_2 respectively, indicating the model’s primary source of doubt about safe-class images is whether they might be moderate DR. For true Grade 3, the epistemic mass is split between C_2 (40.2%) and C_3 (22.7%), reflecting the severity continuum. Grade 2 is also the dominant epistemic class ($\arg \max_k C_k$) for 64.9% of all test samples, confirming that moderate DR is the model’s primary source of confusion at the individual-input level as well.

¹We also evaluated a binary cross-boundary MI variant (MI computed on the binary safe-vs-critical partition), which achieves AUSC 0.284 ± 0.015 , essentially tied with C_{crit_max} (mutual win rate 49.5%/50.5%). It is excluded from the main comparison because it is not part of the C_k framework and exhibits numerical instability (NaN values when $\mu_{\text{safe}} \approx 0$ or $\mu_{\text{safe}} \approx 1$).

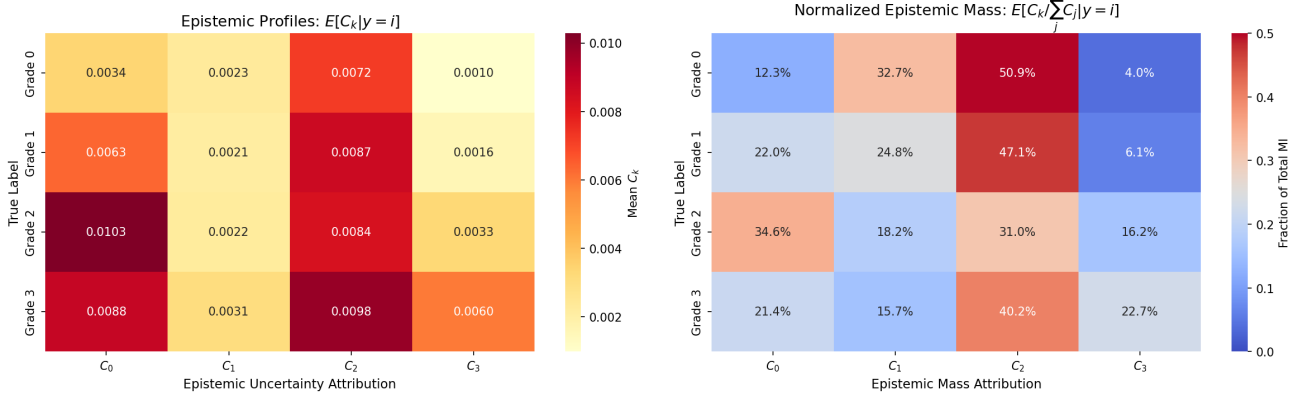


Figure 6: Epistemic profiles. **Left:** Raw $\mathbb{E}[C_k | y=i]$. **Right:** Normalised $\mathbb{E}[C_k / \sum_j C_j | y=i]$. Grade 2 dominates the epistemic budget across all true classes, identifying moderate DR as the model’s primary source of confusion.

D.9 ERROR SIGNATURES

A distinctive advantage of $C(x)$ over scalar MI is that it fingerprints the *structure* of model confusion. Figure 7 shows $\mathbb{E}[C_k | y=i, \hat{y}=j]$ for five clinically important outcomes, and Table 11 provides the numerical values.

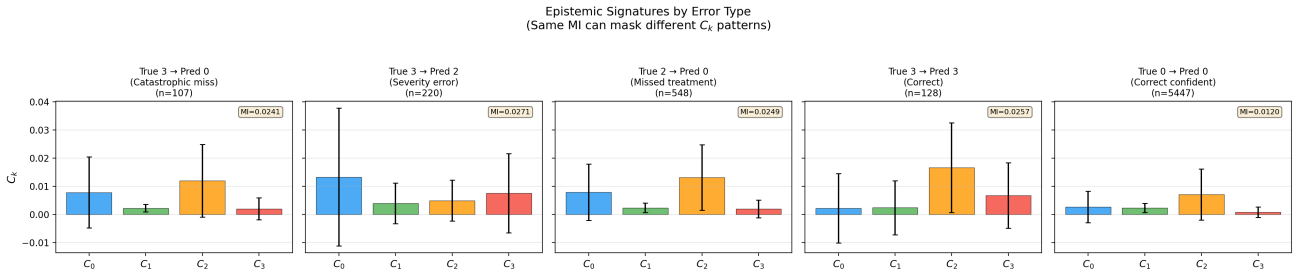


Figure 7: Epistemic signatures of error types. Each bar shows $\mathbb{E}[C_k | y=i, \hat{y}=j]$ for class $k \in \{0, 1, 2, 3\}$. Catastrophic misses ($3 \rightarrow 0$) and severity errors ($3 \rightarrow 2$) have similar MI but distinct C_k fingerprints, revealing different confusion pathways invisible to scalar metrics.

Table 11: Error epistemic signatures: $\mathbb{E}[C_k | y=i, \hat{y}=j]$ for key error types. Errors with nearly identical scalar MI exhibit strikingly different C_k profiles, revealing distinct confusion pathways that suggest different remediation strategies.

Error	n	MI	C_0	C_1	C_2	C_3	Dominant
$3 \rightarrow 0$ (catastrophic)	107	0.024	0.008	0.002	0.012	0.002	C_2
$3 \rightarrow 2$ (severity)	220	0.027	0.013	0.004	0.005	0.008	C_0
$2 \rightarrow 0$ (missed treat.)	548	0.025	0.008	0.002	0.013	0.002	C_2
$3 \rightarrow 3$ (correct)	128	0.026	0.002	0.002	0.017	0.007	C_2
$0 \rightarrow 0$ (correct conf.)	5447	0.012	0.003	0.002	0.007	0.001	C_2

The key interpretability result is that errors with similar scalar MI have distinctive C_k fingerprints. Catastrophic misses (true Grade 3 predicted as Grade 0, $n=107$) and severity underestimates (true Grade 3 predicted as Grade 2, $n=220$) have nearly identical scalar MI (0.024 vs. 0.027 nats) but strikingly different C_k signatures. The catastrophic miss concentrates epistemic mass on C_2 : the model does not jump directly from severe to healthy, but routes through moderate DR, identifying Grade 2 as the “bottleneck” of confusion. The severity underestimate instead elevates C_0 , indicating the model’s primary doubt is whether the image might be healthy. These qualitatively different failure modes, invisible to any scalar metric, suggest distinct intervention strategies: additional moderate-vs-severe training data for the first, and better healthy-vs-severe discrimination for the second.

D.10 EPISTEMIC CONFUSION MATRIX

Figure 8 visualises the epistemic confusion matrix $E_{ij} = \mathbb{E}[\sqrt{C_i C_j} \max(0, -\rho_{ij})]$, which quantifies pairwise confusion between classes using the same correlation-gated geometric mean that underlies CBEC (Eq. 14). Table 12 provides the numerical values.

The cross-boundary block (safe×critical) dominates: its mean value is $2.7\times$ the within-safe mean and $10.6\times$ the within-critical mean, confirming that the model’s epistemic uncertainty concentrates at the clinically dangerous boundary. The strongest pairwise confusion is Grade 0↔Grade 2 (5.08×10^{-3}), consistent with the epistemic profiles (Table 10) showing Grade 2 as the dominant source of uncertainty for healthy images. This structure validates both the safe/critical partition and the CBEC aggregation, which specifically targets cross-boundary confusion.

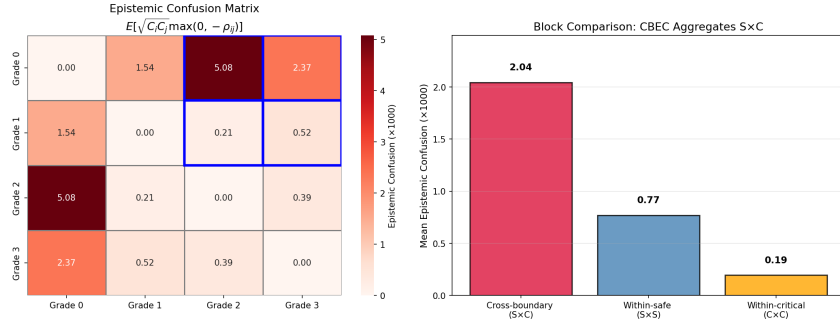


Figure 8: Epistemic confusion matrix $E_{ij} = \mathbb{E}[\sqrt{C_i C_j} \max(0, -\rho_{ij})]$. The cross-boundary block (safe×critical, blue outline) dominates, with the Grade 0↔Grade 2 pair (5.08×10^{-3}) exhibiting the strongest confusion. Within-critical confusion is an order of magnitude weaker ($10.6\times$ smaller mean), confirming that the model’s epistemic uncertainty concentrates at the clinically dangerous safe/critical boundary.

Table 12: Epistemic confusion matrix ($\times 10^3$, Bayesian model). Horizontal rule separates the safe (Grades 0–1) and critical (Grades 2–3) partitions; entries in the off-diagonal blocks constitute the cross-boundary confusion aggregated by CBEC.

	Gr. 0	Gr. 1	Gr. 2	Gr. 3
Grade 0	0.00	1.54	5.08	2.37
Grade 1	1.54	0.00	0.21	0.52
Grade 2	5.08	0.21	0.00	0.39
Grade 3	2.37	0.52	0.39	0.00

D.11 FULL BOOTSTRAP RESULTS: MC DROPOUT

Table 13 reports the MC dropout evaluation. The ranking reversal relative to the BNN (Table 8) is consistent with both the skewness analysis (Appendix D.4) and the findings of Smith and Gal [2018], who showed that MC dropout underestimates posterior uncertainty and creates regions of spurious confidence. The coarser posterior samples inflate ρ_k for critical classes, degrading the reliability of individual C_k values and hence $C_{\text{crit_max}}$, while leaving CBEC’s correlation-gated structure intact, since CBEC computes correlations directly from the MC draws rather than relying on the second-order approximation.

CBEC reduces AUSC by 53.6% relative to MI (0.197 vs. 0.425) and wins 100% of bootstrap samples. Scalar entropy (0.249) outperforms all per-class epistemic methods including MI (0.425) under MC dropout; this is because entropy captures total uncertainty (aleatoric + epistemic), and under MC dropout’s coarser posterior, the aleatoric component carries complementary signal that pure epistemic measures miss. $C_{\text{crit_max}}$ still outperforms its unnormalised counterpart Sale_EU_crit (0.419 vs. 0.463), confirming that the $1/\mu_k$ normalisation provides benefit even when the Taylor approximation is degraded.

Why C_k degrades under MC dropout: a skewness analysis. Figure 10 reveals the mechanism behind $C_{\text{crit_max}}$ ’s ranking reversal. Under the low-rank BNN, the fraction of samples with reliable C_k ($\rho_k < 0.3$) remains above 80% for Grades 0–2

Table 13: Full bootstrap results for MC Dropout ($p=0.3$, $S=30$, 200 resamples). CBEC achieves the lowest AUSC, winning 100% of bootstrap samples, while $C_{\text{crit_max}}$ drops to fifth place. The ranking reversal relative to Table 8 reflects MC dropout’s inflated skewness for critical classes (Figure 10).

Family	Policy	AUSC↓	Critical FNR @80%↓	Acc @80%↑
Boundary	CBEC	0.197 ± 0.012	0.316 ± 0.015	0.867 ± 0.004
Scalar	Entropy	0.249 ± 0.017	0.294 ± 0.014	0.871 ± 0.004
Scalar	MaxProb	0.268 ± 0.017	0.340 ± 0.016	0.874 ± 0.004
Per-class var.	Sale_EU_global	0.364 ± 0.022	0.410 ± 0.018	0.870 ± 0.004
Per-class C_k	$C_{\text{crit_max}}$	0.419 ± 0.025	0.390 ± 0.017	0.854 ± 0.004
Per-class var.	Var_crit	0.424 ± 0.026	0.451 ± 0.018	0.868 ± 0.004
Scalar	MI	0.425 ± 0.024	0.459 ± 0.019	0.864 ± 0.004
Per-class C_k	$C_{\text{crit_sum}}$	0.436 ± 0.026	0.404 ± 0.017	0.860 ± 0.004
Per-class var.	Sale_EU_crit	0.463 ± 0.027	0.527 ± 0.019	0.866 ± 0.004
Per-class MI	OvA_MI	0.526 ± 0.028	0.556 ± 0.020	0.861 ± 0.004

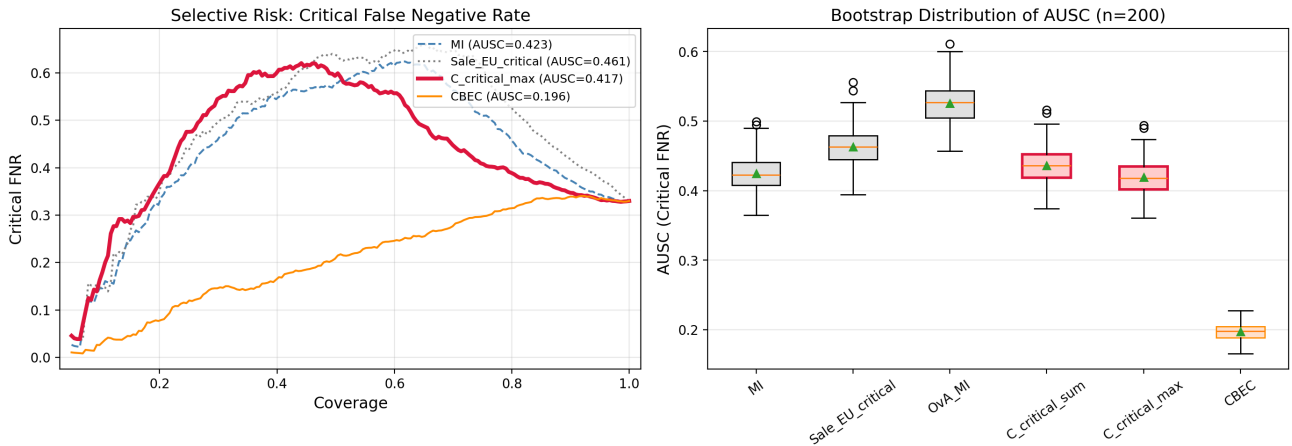


Figure 9: MC dropout selective prediction on diabetic retinopathy. **Left:** Critical FNR vs. coverage curves. CBEC (orange) dominates at all coverage levels; $C_{\text{crit_max}}$ (red) matches MI at low coverage but diverges at mid-range. **Right:** Bootstrap distribution of AUSC ($n=200$). CBEC achieves the lowest AUSC with the tightest spread; $C_{\text{crit_max}}$ and MI are statistically indistinguishable.

and drops to 63% only for Grade 3 (Severe/PDR), the rarest and most difficult class. Under MC dropout, the same statistic degrades monotonically with clinical severity: 88% (Grade 0), 72% (Grade 1), 54% (Grade 2), and only 22% (Grade 3).

The right panel quantifies the gap. Median ρ_k is comparable between the two models at Grade 0 (0.013 vs. 0.012), where both posteriors are well-behaved. The gap widens progressively: at Grade 1, MC dropout’s median ρ_k is $3.5\times$ higher than the BNN’s (0.130 vs. 0.037); at Grade 2 it is $2.1\times$ higher (0.264 vs. 0.124); and at Grade 3 the MC dropout median exceeds the reliability boundary entirely (1.125 vs. 0.218). For the most safety-critical class, more than three quarters of MC dropout samples operate in the regime where the second-order Taylor approximation has broken down. This pattern is consistent with MC dropout’s known tendency to underestimate tail variance [Smith and Gal, 2018]: the resulting predictive distributions are more concentrated than the true posterior, but with heavier skewness, pushing ρ_k above the reliability threshold precisely for the classes that matter most.

These results provide direct empirical support for the complementarity claimed in Section 3: $C_{\text{crit_max}}$ is the preferred deferral metric under well-calibrated posteriors where ρ_k remains low, while CBEC provides a robust fallback when the posterior approximation inflates skewness beyond the Taylor regime. The skewness diagnostic ρ_k therefore serves as a practical model-selection criterion: if median ρ_k for the critical classes exceeds 0.3, practitioners should prefer CBEC over $C_{\text{crit_max}}$.

Figure A1 — C_k Reliability: MC Dropout vs BNN
 MC Dropout degrades C_k most severely for Grade 3: only 22.4% reliable (BNN: see right panel)

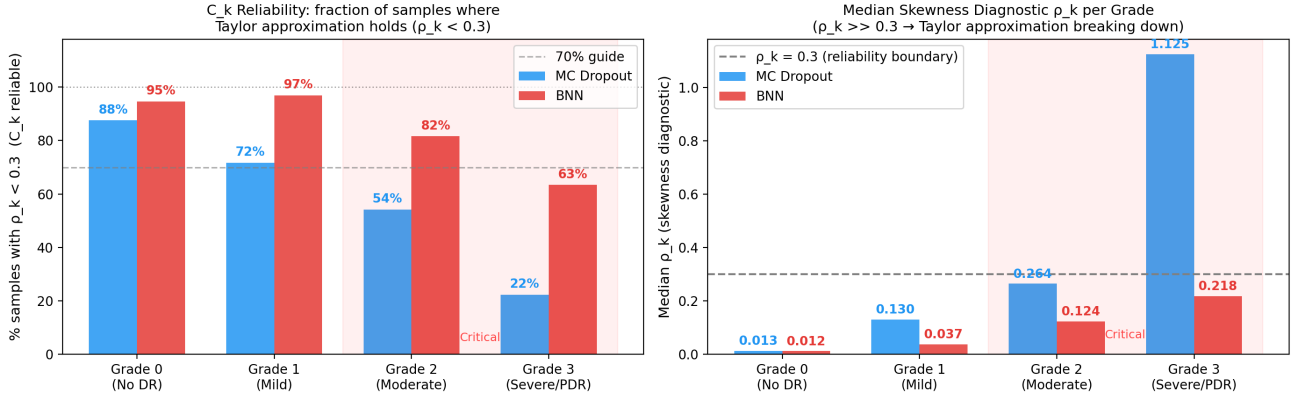


Figure 10: C_k reliability comparison: MC dropout vs. low-rank BNN on diabetic retinopathy. **Left:** Fraction of test samples with $\rho_k < 0.3$ (reliable C_k) per DR grade. The BNN maintains reliability above 60% for all grades; MC dropout drops to 22% for Grade 3. Dashed line: 70% guide. **Right:** Median skewness diagnostic ρ_k per grade. MC dropout exceeds the $\rho_k = 0.3$ reliability boundary at Grade 3 (median 1.125), while the BNN remains below it (0.218). Critical grades (2, 3) are shaded.

D.12 DEEP ENSEMBLE VALIDATION: PER-CLASS METRICS

To verify that the benefit of the $1/\mu_k$ normalisation persists across inference paradigms, we evaluate a deep ensemble of five members on the same diabetic retinopathy test set (7,948 images), using the identical evaluation pipeline. Each member shares the Phase 1 EfficientNet-B4 backbone and is fine-tuned independently with a different random seed; diversity arises from head initialisation rather than stochastic inference. We restrict the comparison to MI as the scalar epistemic reference and the full per-class family: raw per-class variance baselines from Sale et al. [2024] and our proposed C_k metrics.

Reliability. The deep ensemble achieves near-uniform C_k reliability across all DR grades: 95.7%, 91.2%, 91.5%, and 85.1% of samples satisfy $\rho_k < 0.3$ for Grades 0–3 respectively. This places the ensemble firmly in the high-reliability regime, in contrast to MC dropout where Grade 3 reliability collapses to 22% (Figure 10).

Results. Table 14 reports AUSC and critical FNR at 80% coverage over 200 bootstrap resamples.

Table 14: Deep ensemble: per-class metrics. AUSC and critical FNR at 80% coverage (\downarrow better); 200 bootstrap resamples.

Policy	AUSC \downarrow	Crit. FNR @80% \downarrow
Var_crit	0.408 \pm 0.030	0.362 \pm 0.017
Sale_EU_crit [Sale et al., 2024]	0.447 \pm 0.031	0.414 \pm 0.018
C_{crit_max}	0.390 \pm 0.029	0.314 \pm 0.016
C_{crit_sum}	0.406 \pm 0.029	0.333 \pm 0.016
CBEC	0.223 \pm 0.018	0.237 \pm 0.013

Two findings are consistent across all three inference regimes. First, C_{crit_max} outperforms its unnormalised counterpart Sale_EU_crit by 12.9% in AUSC (0.390 vs. 0.447), confirming that the $1/\mu_k$ normalisation provides a systematic advantage over raw per-class variance regardless of the inference method. Second, CBEC achieves the lowest AUSC and critical FNR, outperforming MI by 37.0% (0.223 vs. 0.354) and both Sale et al. variants on every metric. Notably, all three proposed C_k metrics outperform Sale_EU_crit, their direct unnormalised counterpart, confirming the boundary-correction benefit of the $1/\mu_k$ normalisation even in the high-reliability ensemble regime where the Taylor approximation is near-exact ($\sum_k C_k / MI = 0.996$ on this test set).

E OOD DETECTION EXPERIMENT: SUPPLEMENTARY DETAILS

E.1 DATASETS AND PREPROCESSING

FashionMNIST \rightarrow **KMNIST**. FashionMNIST [Xiao et al., 2017] comprises 60,000 grayscale images (28×28) across 10 clothing categories; in code, the 60,000 training images are split into 50,000 train and 10,000 validation, and the standard 10,000 FashionMNIST test set is used as the in-distribution test set. KMNIST [Clanuwat et al., 2018] provides 10,000 test images of cursive Japanese characters in the same format, used entirely as OoD data. Preprocessing is identical for ID/OoD images: cast to `float32`, normalized by dividing pixel values by 126, and flattened each 28×28 image to a 784-dimensional vector; no data augmentation is used.

MIMIC-III ICU \rightarrow **Newborn**. We extract adult ICU admissions from MIMIC-III [Johnson et al., 2016], yielding 44 clinical features with binary mortality labels, split into train/test = 40,406/4,490. The Newborn unit (5,357 admissions) serves as OoD data. The 44-feature pipeline merges (on `SUBJECT_ID`, `HADM_ID`, `ICUSTAY_ID`): (i) static patient features (including age, ICU LOS, pre-ICU hospital time, gender one-hot), (ii) per-stay mean/std aggregates of mapped vital-sign ITEMIDs, and (iii) per-stay mean/std aggregates of mapped lab ITEMIDs restricted to timestamps within ICU stay. Newborn admissions are excluded from ID data and kept as OoD. Adult-ID preprocessing applies an $8 \times$ IQR outlier filter, plausibility filters (`mean_combined_bp_dia` and `mean_combined_bp_sys` > 10 , `time_at_hosp_pre_ic_admission` > 0), fills missing std-feature entries with 0, then uses median imputation and MinMax scaling fit on train and applied to test/OoD. In the OoD loader used for experiments, newborn age (and weight, if present) are set to the adult-training mean values before evaluation.

E.2 MODEL ARCHITECTURE AND TRAINING

Both tasks use fully connected Bayesian neural networks with ReLU activations and low-rank Gaussian posteriors. Output layers are linear (no activation), trained with logits, and mapped to class probabilities via softmax at inference. All models share the following configuration:

Shared specification. The prior is a scale-mixture Gaussian [Blundell et al., 2015] with $\pi=0.5$, $\sigma_1=1.0$, $\sigma_2=\exp(-6)$. Posterior initialisation is adaptive per layer: $\sigma_w^2 = 2/d_{in}$ for ReLU layers, $2/(d_{in}+d_{out})$ otherwise; damping is 0.55 for $r > 5$ (else 0.32); factor means $A_\mu, B_\mu \sim \mathcal{U}(-a, a)$ with $a = \text{damping} \sqrt{3}(\sigma_w^2/r)^{1/4}$; bias means $b_\mu = 0$; and A_ρ, B_ρ, b_ρ are set to constant $\rho_{init} = \log(\exp(\sigma_{init}) - 1)$ with $\sigma_{init} = 0.09(\sigma_w^2/r)^{1/4}$. All models are trained with Adam at learning rate 10^{-3} .

Per-task details. Table 15 summarises the task-specific hyperparameters.

Table 15: OoD model configurations.

	FashionMNIST	MIMIC-III
Hidden layers	$2 \times 1,200$	2×128
Rank r	25	15
Output classes	10	2
Batch size	128	64
Epochs	50	256
KL schedule	Linear warmup, 10 epochs	Fixed
KL scale	$0 \rightarrow 1/N_{train}$	$0.5/\lceil N_{train}/\text{batch} \rceil$
Class weighting	None	$w_0=1, w_1=1/\text{pos_frac} \approx 11.9$
MC samples S	50	512

Results are reported as mean \pm std over 5 independent training seeds.

E.3 EXTENDED OOD DETECTION RESULTS

Table 16 reports per-metric distributional statistics for both benchmarks. On FashionMNIST, MI and EU_{var} share the same OoD/ID ratio ($5.92\times$) but MI achieves higher AUROC because its absolute values provide better threshold separation. On

MIMIC-III, EU_{var} has the highest ratio ($1.71\times$) yet the lowest AUROC among epistemic measures (0.778), confirming that ratio alone does not determine detection performance when the dynamic range of scores is compressed by boundary suppression.

Table 16: OoD distributional analysis: mean uncertainty and OoD/ID ratio.

Dataset	Metric	Mean (ID)	Mean (OoD)	Ratio \uparrow
FashionMNIST	Neg. MSP	0.0506	0.1043	2.07
	MI	0.0096	0.0569	5.92
	EU_{var}	0.0056	0.0333	5.92
	$\sum_k C_k$	0.0106	0.0677	6.43
MIMIC-III	Neg. MSP	0.2543	0.3150	1.24
	MI	0.0378	0.0598	1.61
	EU_{var}	0.0289	0.0485	1.71
	$\sum_k C_k$	0.0377	0.0601	1.62

Per-class decomposition (MIMIC-III). The binary setting permits direct inspection of per-class contributions: $\sum_k C_k = C_0 + C_1$. Table 17 reveals that distributional shift affects the two classes asymmetrically. The survival class exhibits a $2.15\times$ increase from ID to OoD (C_0 : 0.014 \rightarrow 0.030), while the mortality class shows only $1.30\times$ (C_1 : 0.022 \rightarrow 0.029). The critical-class-only metric C_1 achieves AUROC 0.740 ± 0.074 , substantially below $\sum_k C_k$ at 0.815 ± 0.017 : by focusing exclusively on mortality-class uncertainty, it misses the larger OoD signal carried by C_0 . This illustrates a task-dependent trade-off: $C_{\text{crit_max}}$ targets safety-critical selective prediction (Section 3), where critical-class uncertainty directly determines clinical harm; for general OoD detection, all-class aggregation captures the complete distributional shift.

Table 17: Per-class decomposition on MIMIC-III OoD detection.

Metric	Mean (ID)	Mean (OoD)	Ratio \uparrow	AUROC \uparrow
C_0 (survival)	0.014	0.030	2.15	0.773 ± 0.005
C_1 (mortality)	0.022	0.029	1.30	0.740 ± 0.074
$\sum_k C_k$	0.038	0.060	1.62	0.815 ± 0.017

E.4 PER-CLASS EPISTEMIC DECOMPOSITION FOR FASHIONMNIST

The main text reports $\sum_k C_k$ as the best OoD metric for FashionMNIST \rightarrow KMNIST (AUROC 0.735 ± 0.009) but presents only the scalar aggregate. Figure 11 decomposes this into the ten individual C_k values, revealing which clothing categories drive the OoD signal when the model encounters KMNIST inputs.

Table 18 reports the numerical values for each class. For reference, the aggregate $\sum_k C_k$ achieves an OoD/ID mean-score

Table 18: Per-class mean C_k for FashionMNIST (ID) vs. KMNIST (OoD), averaged over 5 seeds with seed standard deviation. Ratio = $\bar{C}_k^{\text{OoD}}/\bar{C}_k^{\text{ID}}$.

Class	\bar{C}_k^{ID}	σ^{ID}	\bar{C}_k^{OoD}	σ^{OoD}	Ratio
T-shirt/top	0.00140	0.00014	0.00966	0.00064	6.92
Trouser	0.00033	0.00007	0.00517	0.00064	15.65
Pullover	0.00164	0.00013	0.00571	0.00112	3.49
Dress	0.00108	0.00010	0.01015	0.00079	9.37
Coat	0.00156	0.00015	0.00543	0.00106	3.48
Sandal	0.00064	0.00008	0.00920	0.00154	14.43
Shirt	0.00228	0.00019	0.01020	0.00133	4.48
Sneaker	0.00064	0.00007	0.00222	0.00058	3.49
Bag	0.00045	0.00007	0.00840	0.00099	18.67
Ankle boot	0.00056	0.00008	0.00158	0.00058	2.85
$\sum_k C_k$ (aggregate)	0.01056	-	0.06773	-	6.43

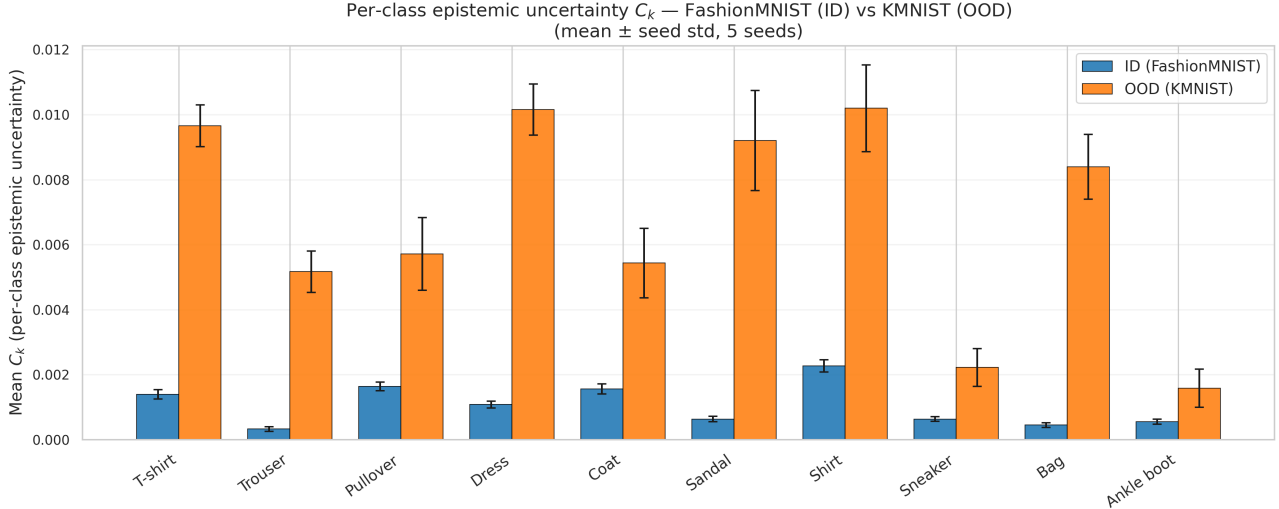


Figure 11: Per-class epistemic uncertainty C_k for each of the ten FashionMNIST categories, comparing ID (FashionMNIST test, $N = 10,000$) vs. OoD (KMNIST test, $N = 10,000$) samples. Bars: mean over 5 seeds; error bars: seed standard deviation. All ten classes show $C_k^{\text{OoD}} > C_k^{\text{ID}}$, though the magnitude varies considerably (Bag: $18.7\times$; Ankle boot: $2.8\times$; Table 18). The OoD signal is *consistent in direction* across all categories but not uniform in magnitude, suggesting that KMNIST activates some FashionMNIST class representations more than others.

ratio of $6.43\times$ (vs. $5.92\times$ for MI and $5.92\times$ for EU_{var}), confirming that the μ_k -normalisation in C_k provides a consistent boost over the raw variance sum.

E.5 SCORE DISTRIBUTION ANALYSIS AND THE EU_{var} PARADOX

On MIMIC-III, EU_{var} achieves the *highest* mean OoD/ID ratio ($1.705\times$) yet the *lowest* AUROC (0.778) among the three primary Bayesian metrics. Figure 12 makes this paradox immediately visual.

Why a high mean ratio does not imply better separability. AUROC measures $P(s_{\text{OoD}} > s_{\text{ID}})$ for a randomly chosen pair drawn independently from the OoD and ID score distributions. This probability is governed by the *full distributional overlap*, not merely the ratio of means. Under a Gaussian approximation of the log-scores, the relationship is

$$\text{AUROC} \approx \Phi\left(\frac{\mu_{\text{OoD}} - \mu_{\text{ID}}}{\sqrt{\sigma_{\text{OoD}}^2 + \sigma_{\text{ID}}^2}}\right), \quad (53)$$

where Φ is the standard-normal CDF. A high OoD/ID mean ratio inflates the numerator, but if the within-group standard deviations are also large, the denominator grows proportionally and the AUROC gain is suppressed, analogous to Cohen’s d .

Why EU_{var} suffers from dynamic range compression. $EU_{\text{var}} = \sum_k \text{Var}[p_k]$ is an un-normalised variance sum. For a sigmoid binary classifier, predictive variance is *heteroscedastic*: samples near the decision boundary have high $\text{Var}[p_k]$ irrespective of ID/OoD status, simultaneously inflating the right tail of *both* distributions. Although the OoD mean exceeds the ID mean by a factor of $1.71\times$, the bulk of both distributions concentrates near zero with only a thin right tail separating them. The resulting large within-group spread keeps the denominator of (53) large, yielding the lowest AUROC (0.778) among the three Bayesian metrics.

Why $\sum_k C_k$ achieves better separation with a lower ratio. $C_k = \text{Var}[p_k] / (2\mu_k)$ normalises each variance component by the corresponding mean probability. This acts as a variance-stabilising transform: large absolute variances that arise when μ_k is also large are down-weighted, while contributions from classes with small μ_k are amplified. The net effect narrows the within-group spread for both ID and OoD populations, so a smaller mean ratio ($1.62\times$ vs. $1.71\times$) still translates to cleaner tail separation and a higher AUROC (0.815).

MIMIC: ID (ICU) vs OOD (Newborn) score distributions
Dashed lines = means; shaded = histogram; curves = KDE

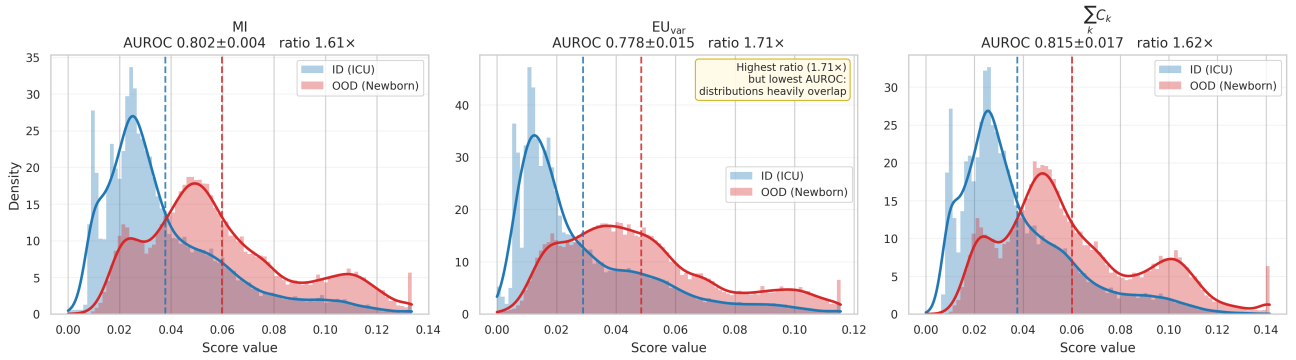


Figure 12: MIMIC ICU (blue) vs. Newborn (red) score distributions for the three primary Bayesian metrics, pooled across 5 seeds ($\approx 22,000$ ID samples, $\approx 27,000$ OoD samples). Shaded areas: histograms (90 bins, density-normalised). Solid curves: kernel density estimates (Scott’s rule). Dashed verticals: distribution means. **Centre panel:** despite achieving the largest mean separation ($1.705\times$), both ID and OoD EU_{var} distributions concentrate near zero with a shared heavy right tail. **Right panel:** $\sum_k C_k$ achieves better tail separation, yielding the highest AUROC (0.815).

Why the paradox is absent on FashionMNIST. On FashionMNIST \rightarrow KMNIST, EU_{var} and MI attain nearly identical mean ratios ($5.923\times$ vs. $5.921\times$), and their AUROC gap is only 0.014. The distinction arises because KMNIST induces a strong, directionally consistent uncertainty lift across all ten softmax outputs, preventing the range compression that afflicts EU_{var} on MIMIC’s binary sigmoid output.

E.6 EMPIRICAL VERIFICATION OF THE SKEWNESS DIAGNOSTIC

Lemma 2.9 establishes that the expected entropy satisfies

$$\mathbb{E}[\mathcal{H}(\mathbf{p})] \approx \mathcal{H}(\boldsymbol{\mu}) - \frac{1}{2} \sum_k \frac{\text{Var}[p_k]}{\mu_k} + \frac{1}{6} \sum_k \frac{m_{3,k}}{\mu_k^2}, \quad (54)$$

where $m_{3,k} = \frac{1}{S} \sum_{s=1}^S (p_k^{(s)} - \mu_k)^3$ is the empirical third central moment. The reliability of the second-order approximation (i.e. $\sum_k C_k$) is governed by the skewness diagnostic

$$\rho_k(x) = \frac{|m_{3,k}|}{3 \mu_k \cdot \text{Var}[p_k]} = \frac{|\text{3rd-order correction}|}{|\text{2nd-order correction}|}, \quad (55)$$

so $\rho_k < 1$ signals a reliable quadratic regime and $\rho_k \gg 1$ signals regime breakdown. Note that $3\mu_k \cdot \text{Var}[p_k] = 6\mu_k^2 C_k$, so $\rho_k = |m_{3,k}| / (6\mu_k^2 C_k)$: the $1/\mu_k^2$ factor amplifies ρ_k for classes with small predicted probability, which is precisely the singularity avoided by using C_k rather than $C_k^{(3)}$.

The main text claims OoD inputs have higher ρ_k than ID inputs. Figures 13 and 14 provide the first direct empirical confirmation, with one instructive exception.

Table 19: MIMIC: median and mean of ρ_k for ID (ICU) and OoD (Newborn) populations, pooled across 5 seeds. Mann–Whitney U test, two-sided.

Class	Median		Mean		MWU p	Direction
	ID	OoD	ID	OoD		
ρ_0 (survive)	0.032	0.046	0.142	0.222	$< 10^{-300}$	OoD > ID ✓
ρ_1 (mortality)	0.079	0.065	0.099	0.080	$< 10^{-130}$	OoD < ID ✗

MIMIC-III ($K = 2$).

Skewness diagnostic $\rho_k = |m_{3,k}| / (3\mu_k \text{Var}[p_k])$ — ID vs OoD (pooled 5 seeds)
Dashed lines = medians. Higher $\rho_k \Rightarrow$ larger 3rd-order correction \Rightarrow quadratic C_k less reliable.

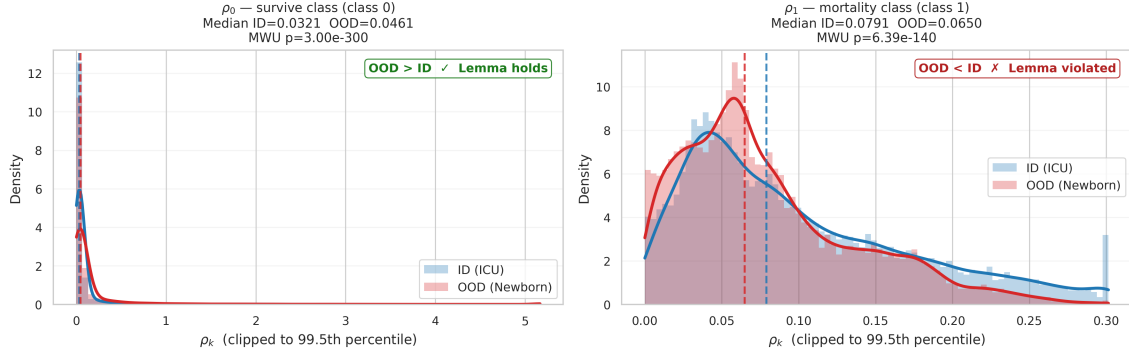


Figure 13: Skewness diagnostic ρ_k for ID (ICU, blue) and OoD (Newborn, red) on MIMIC, pooled across 5 seeds. Shaded areas: density-normalised histograms clipped to the 99.5th percentile; solid curves: kernel density estimates; dashed verticals: medians. **Left (ρ_0 , survive):** Both distributions concentrate well below 0.3, confirming that C_0 is reliable for both populations; the median shift (0.032 \rightarrow 0.046) is statistically significant but practically small. **Right (ρ_1 , mortality):** The OoD distribution shifts *left* (median 0.065 < 0.079), reversing the pattern predicted by Lemma 2.9; near-zero μ_1 for newborns collapses $\text{Var}[p_1]$ faster than $1/\mu_1$ compensates, concentrating the third-order signal in class 0.

The ρ_1 reversal on MIMIC. The mortality class ($k=1$) shows the *opposite* direction to the Lemma 2.9 prediction: OoD newborns have *lower* ρ_1 than ICU patients (median 0.065 < 0.079, $p < 10^{-130}$). The mechanism is coherent: the model learns to predict near-zero mortality probability for newborns, a structurally healthy population. Consequently, all $S = 512$ MC samples pile up near $p_1 \approx 0$, producing a distribution over p_1 that is *tight* (small $\text{Var}[p_1]$) and slightly right-skewed, so the third central moment $|m_{3,1}|$ collapses faster than the $1/\mu_1$ amplification in the denominator of ρ_1 can compensate. The OoD detection signal for MIMIC lives entirely in class 0 (survive): ρ_0 shifts right by 43% on the median.

Crucially, this does not contradict higher epistemic uncertainty for OoD inputs. Because $C_k = \text{Var}[p_k] / (2\mu_k)$, a smaller $\text{Var}[p_1]$ and a simultaneously smaller μ_1 can still yield a larger C_1 : for OoD newborns, μ_1 collapses faster than $\text{Var}[p_1]$, so $C_1^{\text{OoD}} > C_1^{\text{ID}}$ (Table 17) even while $\text{Var}[p_1]^{\text{OoD}} < \text{Var}[p_1]^{\text{ID}}$. The μ_k normalisation in C_k is precisely what decouples epistemic uncertainty from MC spread, and it is the MC spread, not C_k , that governs ρ_k .

The reversal is not specific to MIMIC or to minority classes. The correct sufficient condition is: *the MC draws are more consistent about p_k for OoD samples than for ID samples*, i.e. $\text{Var}[p_k]^{\text{OoD}} < \text{Var}[p_k]^{\text{ID}}$. The ρ_1 reversal does not invalidate Lemma 2.9, which makes no per-class monotonicity claim, but it highlights that binary-output models can concentrate their third-order regime into a single class depending on the OoD population’s characteristics.

Table 20: FashionMNIST: per-class mean ρ_k for ID and OoD populations, averaged over 5 seeds, with Mann–Whitney U p -values computed on pooled samples ($5 \times 10,000$ per split per class).

Class	$\bar{\rho}_k^{\text{ID}}$	σ^{ID}	$\bar{\rho}_k^{\text{OoD}}$	σ^{OoD}	MWU p	OoD/ID
T-shirt/top	0.04333	0.00476	0.28470	0.01950	≈ 0	6.57
Trouser	0.01426	0.00494	0.17139	0.01775	≈ 0	12.02
Pullover	0.05121	0.00506	0.19319	0.02847	8×10^{-260}	3.77
Dress	0.03375	0.00451	0.25126	0.01659	≈ 0	7.45
Coat	0.04594	0.00462	0.17652	0.02213	7×10^{-264}	3.84
Sandal	0.01726	0.00182	0.24578	0.03093	≈ 0	14.24
Shirt	0.06693	0.00777	0.27297	0.02592	≈ 0	4.08
Sneaker	0.01728	0.00344	0.08564	0.02328	3×10^{-56}	4.96
Bag	0.01688	0.00236	0.23378	0.02085	≈ 0	13.85
Ankle boot	0.01832	0.00397	0.06293	0.02174	5×10^{-13}	3.43

FashionMNIST ($K = 10$).

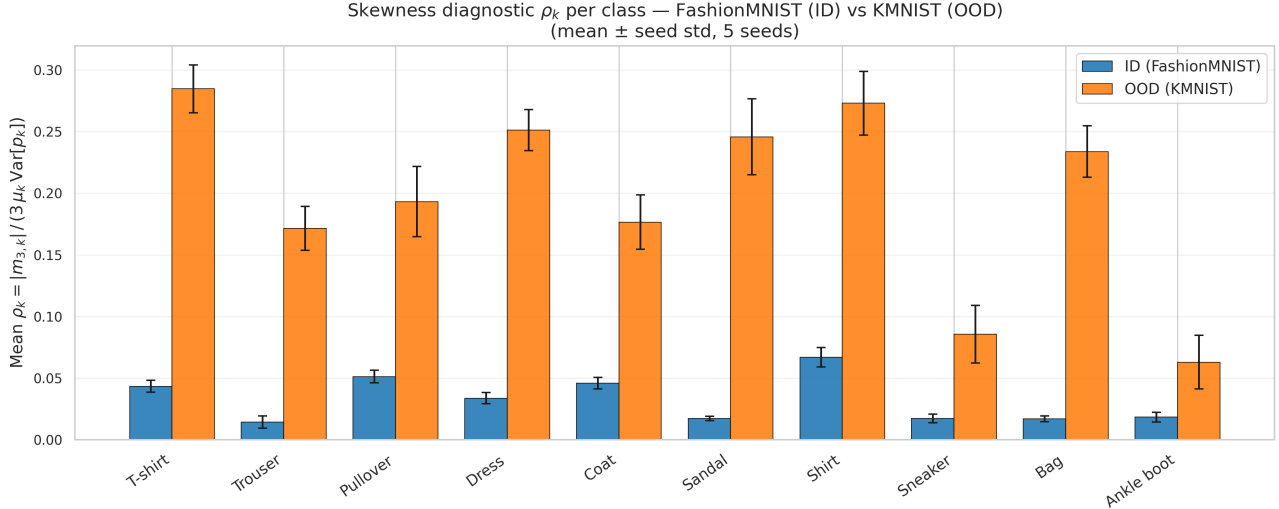


Figure 14: Per-class skewness diagnostic ρ_k for FashionMNIST (ID, blue) vs. KMNIST (OoD, orange), averaged over 5 seeds. Error bars: seed standard deviation. All ten categories show $\rho_k^{\text{OoD}} > \rho_k^{\text{ID}}$, confirming that KMNIST inputs produce systematically more asymmetric MC posteriors across every class, with OoD/ID ratios ranging from $3.4\times$ (Ankle boot) to $14.2\times$ (Sandal). The directional pattern is consistent with the C_k profile (Figure 11), though the per-class rankings differ, as ρ_k depends on third-moment structure rather than variance alone.

Interpretation. These figures close the loop between Lemma 2.9 and the empirical OoD results. OoD inputs are not merely *more uncertain* (higher C_k) but more *asymmetrically uncertain* (higher ρ_k), at least for classes where the OoD population has meaningful predicted probability mass. When $\rho_k \ll 1$ (ID regime), the second-order approximation is trustworthy and $\sum_k C_k \approx \text{MI}$, so the two metrics converge. When ρ_k is large (OoD regime), the cubic correction in (54) becomes significant; $\sum_k C_k$ captures this additional signal through its $1/\mu_k$ weighting, while MI averages over the sampling distribution without per-class amplification. On FashionMNIST, where KMNIST induces consistently higher uncertainty across all ten logit outputs, the reversal is absent: every class shows $\rho_k^{\text{OoD}} > \rho_k^{\text{ID}}$ (Figure 14).

E.7 DEEP ENSEMBLE OOD DETECTION: MIMIC-III

We repeat the MIMIC-III ICU \rightarrow Newborn OoD detection experiment using a deep ensemble of five members (one deterministic forward pass per member) in place of the low-rank Bayesian model. The ensemble uses the same 44-feature pipeline and identical evaluation code; uncertainty is derived from disagreement across members rather than MC sampling. As the ensemble consists of a single trained instance, no seed standard deviation is reported.

Table 21: OoD detection on MIMIC-III ICU \rightarrow Newborn: deep ensemble. AUROC and OoD/ID mean-score ratio. Best in **bold**.

Method	AUROC \uparrow	Ratio \uparrow
Neg. MSP	0.701	1.68
MI	0.752	2.32
EU_{var}	0.750	2.72
$\sum_k C_k$	0.753	2.31

The ranking $\sum_k C_k > \text{MI} > EU_{\text{var}}$ mirrors the low-rank Bayesian result (Table 3). Critically, EU_{var} again achieves the highest OoD/ID ratio ($2.72\times$) yet the lowest AUROC among epistemic measures: without mean-normalisation, boundary suppression compresses the dynamic range of scores, so a numerically large mean shift is swamped by within-group spread, failing to produce separable distributions. $\sum_k C_k$ corrects this via the $1/\mu_k$ weighting, yielding the highest AUROC across both inference regimes.

F EPISTEMIC SENSITIVITY TO DATA QUALITY: SUPPLEMENTARY DETAILS

F.1 MODEL ARCHITECTURE AND TRAINING

Both end-to-end models use low-rank Gaussian posteriors with the shared specification described in Appendix E.2.

Fashion-MNIST. Fully connected Bayesian network, two hidden layers of 400 units, rank 15, ReLU activations. Trained for 50 epochs with Adam ($\text{lr} = 10^{-3}$), batch size 128, $S=50$ MC samples at inference.

CIFAR-10 (from scratch). CNN with Conv $32 \rightarrow 64 \rightarrow 128$, each followed by ReLU and 2×2 max-pooling, global average pooling, and a low-rank Bayesian head (rank 32). Trained for 100 epochs with Adam ($\text{lr} = 10^{-3}$), batch size 128, $S=50$ MC samples at inference.

Label noise injection. For each noise rate $\alpha \in \{0.1, 0.2, 0.3, 0.4, 0.5\}$, a fraction α of training labels is replaced uniformly at random across all classes. The test set remains clean throughout. Models are retrained from scratch at each noise level; results are mean over 5 seeds.

F.2 TRANSFER LEARNING EXPERIMENTS

To isolate the effect of end-to-end Bayesian training, we repeat the disentanglement protocol with a frozen ImageNet-pretrained ResNet-50 backbone, replacing only the classifier head with one of three Bayesian variants:

- **Low-rank variational** (rank = 32, constrained posterior),
- **Full-rank variational** (unconstrained Bayesian weight distributions),
- **MC Dropout** ($p=0.3$, deterministic weights with dropout-based uncertainty).

This design enables a controlled comparison: CIFAR-10 from scratch vs. CIFAR-10 transfer uses the *same dataset*, *same K* , and *same Bayesian model type* (low-rank), isolating the training regime as the causal variable.

Why a relative ratio. The naive absolute ratio $R_{\text{abs}}(\alpha) = (\bar{U}_e(\alpha) - \bar{U}_e(0)) / (\bar{U}_a(\alpha) - \bar{U}_a(0))$ is confounded by the scale of epistemic uncertainty. Low-rank models produce baseline MI an order of magnitude below their full-rank counterparts (0.007 vs. 0.039 on CIFAR-10; Table 22), so the absolute numerator $\bar{U}_e(\alpha) - \bar{U}_e(0)$ is mechanically small regardless of whether the *proportional* increase is large or small. A low-rank model and a full-rank model with identical proportional epistemic leakage would report very different R_{abs} values, making cross-model comparison misleading. The relative formulation R_{rel} (Equation 15) normalises each delta by its own baseline, yielding a scale-invariant elasticity: for every 1% relative increase in aleatoric uncertainty, how many percent does epistemic uncertainty increase? This makes R_{rel} directly comparable across models with different posterior families, rank constraints, and training regimes.

Baseline inflation. Table 22 reports baseline epistemic uncertainty ($\alpha=0$) across all configurations. End-to-end models show negligible inflation of $\sum_k C_k$ over MI (1.0–1.02 \times), while transfer-learning models exhibit progressively higher inflation: low-rank (1.08–1.17 \times), full-rank (1.35–1.59 \times), MC dropout (1.62–1.89 \times). Training regime matters more than dataset: CIFAR-10 low-rank with transfer learning (1.08 \times) shows more inflation than CIFAR-10 low-rank from scratch (1.02 \times) on the *same data*.

Disentanglement ratios: CIFAR-10 transfer. Table 23 shows that under transfer learning MI outperforms $\sum_k C_k$ for the low-rank model at all noise levels ($|R_{\text{rel}}| = 1.83$ vs. 1.97 at $\alpha=0.1$), consistent with the high inflation of this configuration. For full-rank models, $\sum_k C_k$ overtakes MI at $\alpha \geq 0.2$. MC dropout shows the worst overall ratios (0.18–0.90), with $\sum_k C_k$ recovering at high noise ($\alpha \geq 0.4$). The model ordering for disentanglement quality is consistent: low-rank best under end-to-end training but worst under transfer, full-rank intermediate, MC dropout worst overall.

Disentanglement ratios: CIFAR-100 transfer. Table 24 extends the analysis to $K=100$. Low-rank achieves strong disentanglement ($|R_{\text{rel}}| < 0.37$) for both metrics at all noise levels, with $\sum_k C_k$ winning at every α . Full-rank shows MI winning at low noise but $\sum_k C_k$ recovering at $\alpha \geq 0.4$. MC dropout is the worst configuration: MI wins at all noise levels, with ratios exceeding 0.58.

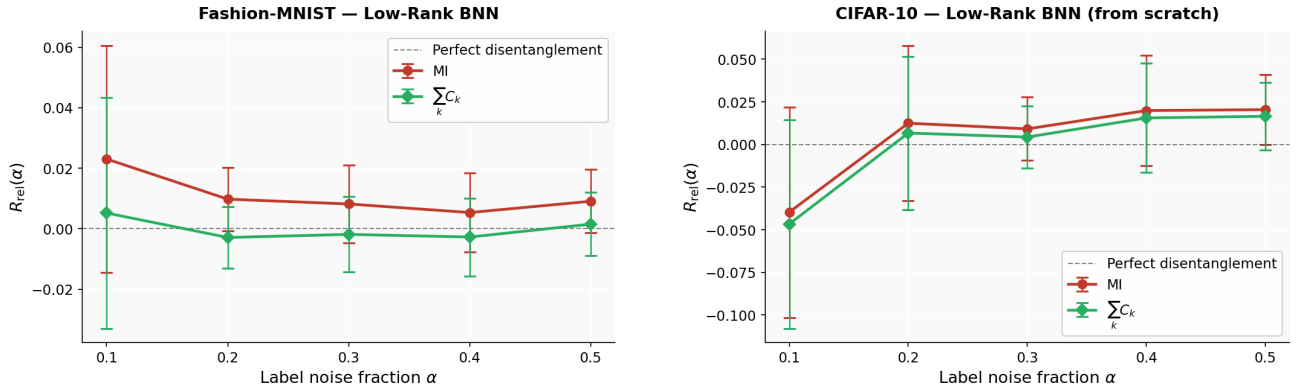


Figure 15: Disentanglement ratios $|R_{\text{rel}}(\alpha)|$ for end-to-end low-rank models. $\sum_k C_k$ (green) is closer to zero than MI (red) at every noise level. **Left:** Fashion-MNIST. **Right:** CIFAR-10.

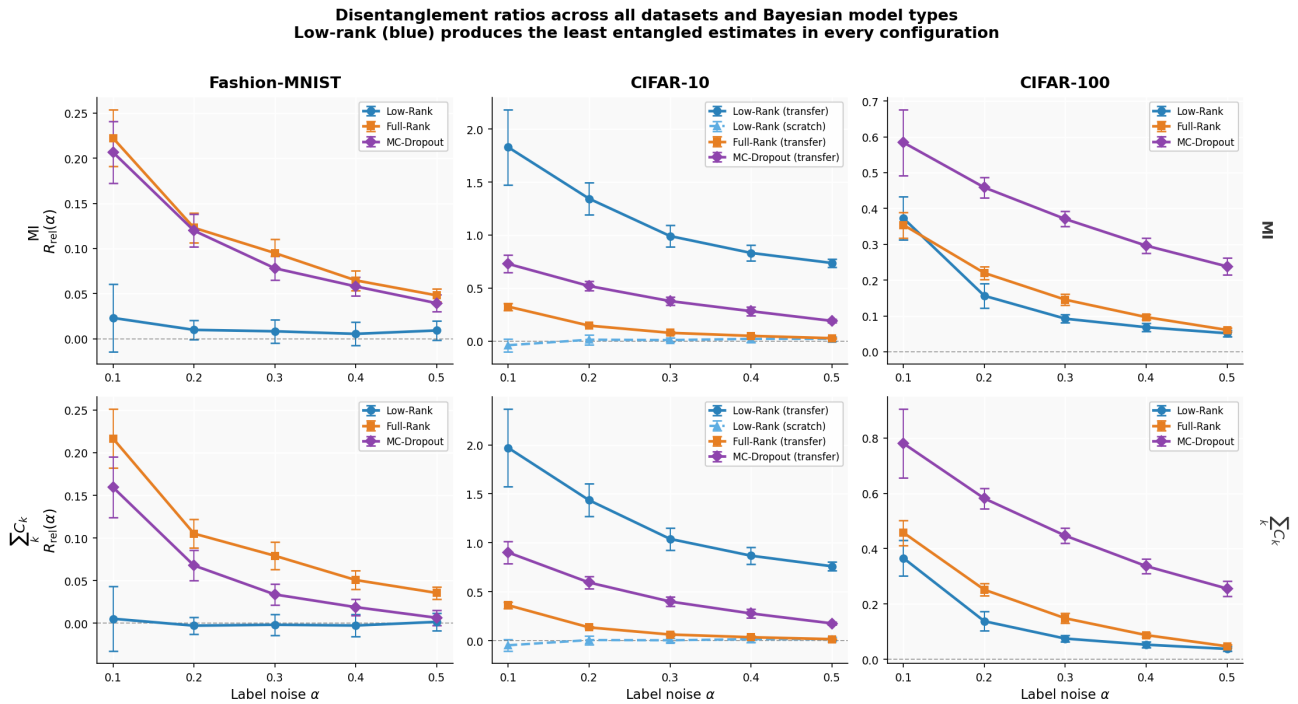


Figure 16: Relative disentanglement ratios $|R_{\text{rel}}(\alpha)|$ across all datasets and Bayesian model types. Top row: MI. Bottom row: $\sum_k C_k$. Low-rank (blue) produces the least entangled estimates in every configuration.

Key patterns across transfer-learning experiments. The controlled comparison on CIFAR-10 is decisive: using the *same dataset* ($K=10$) and *same model type* (low-rank), training from scratch yields $|R_{\text{rel}}| < 0.05$ while transfer learning yields 0.74–1.97. This directly isolates the training regime as a causal factor. Within transfer learning, higher baseline inflation ($\sum_k C_k / \text{MI}$) correlates with worse $\sum_k C_k$ performance relative to MI, a pattern that holds for both CIFAR-10 and CIFAR-100. The implication is that when the entire model participates in the Bayesian posterior, the resulting predictive distributions have a variance structure that is well captured by the C_k normalisation; when only a classifier head is Bayesian, this structure degrades.

Effect of rank constraint on uncertainty scale. The low-rank variational framework of Toure and Stephens [2026] parameterizes each weight matrix as $W = AB^\top$ with independent mean-field Gaussian posteriors $q(A)q(B)$ on the factors $A \in \mathbb{R}^{m \times r}$, $B \in \mathbb{R}^{n \times r}$. The induced posterior on W is *singular* with respect to Lebesgue measure, concentrating entirely on the manifold \mathcal{R}_r of rank- r matrices: every sampled weight matrix is constrained to have rank at most r , though the

Table 22: Baseline epistemic uncertainty ($\alpha=0$, no label noise). Inflation = $\sum_k C_k / \text{MI}$.

Dataset	Model	Training	K	MI	$\sum_k C_k$	Inflation
Fashion-MNIST	Low-rank Bayes	From scratch	10	0.008	0.008	1.00×
CIFAR-10	Low-rank Bayes	From scratch	10	0.0067	0.0069	1.02×
CIFAR-10	Low-rank Bayes	Transfer	10	0.0045	0.0048	1.08×
CIFAR-10	Full-rank Bayes	Transfer	10	0.039	0.053	1.35×
CIFAR-10	MC Dropout	Transfer	10	0.039	0.063	1.62×
CIFAR-100	Low-rank Bayes	Transfer	100	0.042	0.049	1.17×
CIFAR-100	Full-rank Bayes	Transfer	100	0.190	0.302	1.59×
CIFAR-100	MC Dropout	Transfer	100	0.238	0.450	1.89×

Table 23: $|R_{\text{rel}}(\alpha)|$ for CIFAR-10 ($K=10$, transfer learning). Values < 0.3 in **bold**. †: $\sum_k C_k$ outperforms MI.

α	Low-rank		Full-rank		MC Dropout	
	MI	$\sum_k C_k$	MI	$\sum_k C_k$	MI	$\sum_k C_k$
0.1	1.830	1.970	0.325	0.362	0.728	0.901
0.2	1.344	1.435	0.145	0.136 †	0.519	0.594
0.3	0.991	1.039	0.077	0.063 †	0.377	0.400
0.4	0.832	0.868	0.048	0.035 †	0.282	0.278 †
0.5	0.737	0.760	0.026	0.016 †	0.190	0.177 †

Table 24: $|R_{\text{rel}}(\alpha)|$ for CIFAR-100 ($K=100$, transfer learning). Values < 0.3 in **bold**. †: $\sum_k C_k$ outperforms MI.

α	Low-rank		Full-rank		MC Dropout	
	MI	$\sum_k C_k$	MI	$\sum_k C_k$	MI	$\sum_k C_k$
0.1	0.373	0.366 †	0.354	0.458	0.584	0.780
0.2	0.156	0.138 †	0.220	0.252	0.459	0.581
0.3	0.092	0.075 †	0.145	0.149	0.371	0.447
0.4	0.069	0.053 †	0.097	0.088 †	0.296	0.337
0.5	0.052	0.038 †	0.061	0.047 †	0.238	0.256

specific column and row spaces vary across posterior samples. Under the same transfer-learning protocol on CIFAR-10, the low-rank model ($r=32$) produces baseline MI an order of magnitude below its full-rank counterpart (0.0045 vs. 0.039), a gap that persists across all noise levels (e.g., at $\alpha=0.5$: 0.047 vs. 0.072). The from-scratch low-rank model exhibits a similar absolute scale (MI = 0.0067), confirming that the compression is driven primarily by the rank constraint rather than the training regime. This compression has two distinct sources. First, the rank constraint itself restricts the number of independent directions along which weight matrices can vary; the resulting predictive distributions inherit this reduced dimensionality, yielding smaller $\text{Var}[p_k]$ and thus smaller MI. Second, while the factored posterior introduces structured correlations between weight entries ($\text{Cov}(W_{ij}, W_{i'j'}) \neq 0$ whenever the entries share latent factors), it remains mean-field *within* each factor, which is known to underestimate marginal variances relative to the true posterior [Blei et al., 2017, Turner and Sahani, 2011], further concentrating the predictive distribution. Crucially, this compression affects the *absolute scale* of uncertainty but not the *relative ranking* of inputs or the *within-model metric comparison*: since $\sum_k C_k$ and MI share the same compressed scale by construction (Equation 8), their relative disentanglement ratios $R_{\text{rel}}(\alpha)$ remain directly comparable within a given model, and the finding that $\sum_k C_k$ leaks less than MI holds independently of the overall scale. However, uncertainty thresholds calibrated on one posterior family cannot be transferred to another without recalibration, and the small absolute values produced by low-rank models should not be interpreted as evidence of low true epistemic uncertainty but rather as a consequence of both the manifold constraint on the posterior support and the mean-field under-dispersion within the learned factors.

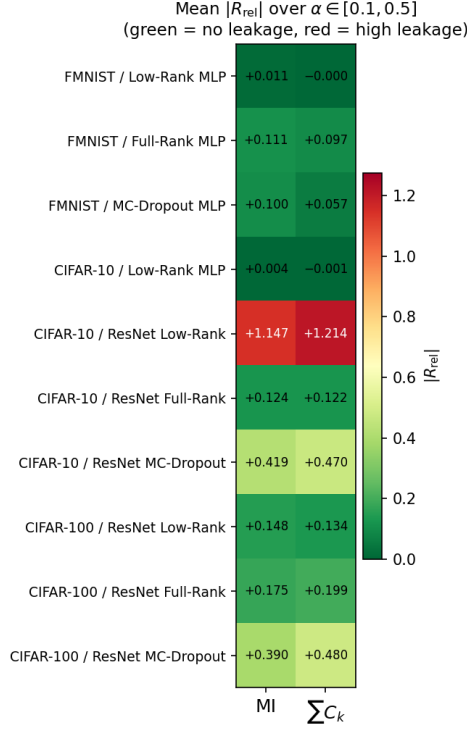


Figure 17: Mean $|R_{\text{rel}}|$ averaged over $\alpha \in \{0.1, \dots, 0.5\}$ for all ten model/dataset combinations. Green indicates near-zero leakage; red indicates high entanglement. End-to-end low-rank models (top rows) achieve the strongest disentanglement for both metrics.

E.3 SENSITIVITY TO CLASS CARDINALITY

The $1/\mu_k$ normalisation that corrects boundary suppression also introduces a scaling effect with the number of classes K . Under the simplex constraint $\sum_k \bar{p}_k = 1$, as K grows the average probability per class decreases. For a model assigning probability α to the predicted class and distributing the remainder uniformly:

$$\bar{p}_k = \frac{1 - \alpha}{K - 1} \quad \text{for } k \neq \text{pred.} \quad (56)$$

Assuming approximately uniform variance $\text{Var}(p_k) \approx \sigma^2$ across classes:

$$\sum_k C_k \approx \frac{\sigma^2}{2\alpha} + \frac{(K - 1)^2 \sigma^2}{2(1 - \alpha)} \sim \mathcal{O}(K^2), \quad (57)$$

whereas MI, measuring entropy differences bounded by $\log K$, does not accumulate linearly over classes.

Empirically, this manifests as higher baseline inflation on CIFAR-100 compared to CIFAR-10 for every model type (Table 22): low-rank $1.17\times$ vs. $1.08\times$; full-rank $1.59\times$ vs. $1.35\times$; MC dropout $1.89\times$ vs. $1.62\times$. The K -dependence interacts with model type: low-rank models remain resilient at $K=100$ ($|R_{\text{rel}}| < 0.37$), while MC dropout fails substantially ($|R_{\text{rel}}|$ up to 0.78 at $\alpha=0.1$).

Mitigation strategies. For high-cardinality settings ($K \gtrsim 50$), two modifications can reduce inflation without sacrificing the per-class interpretability of C_k : (i) *truncated summation*, restricting $\sum_k C_k$ to the top- k most probable classes, which eliminates the accumulation of amplified terms from negligible-probability classes; (ii) *probability-weighted aggregation*, weighting each C_k by μ_k to down-weight low-probability contributions. We recommend reporting both $\sum_k C_k$ and MI in high- K settings: the per-class decomposition retains interpretive value even when the aggregate $\sum_k C_k$ underperforms MI as a scalar summary.